Title
PERMEATION OF SILICATE LIQUIDS INTO SINTERED MAGNESIA COMPACTS

Author
Wong, Boon.

Publication Date
1972-08-01

PERMEATION OF SILICATE LIQUIDS INTO SINTERED MAGNESIA COMPACTS

Boon Wong
(M.S. Thesis)

August 1972

AEC Contract No. W-7405-eng-48

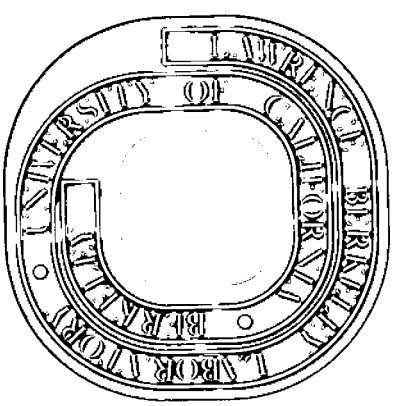

LBL-877

PERMEATION OF SILICATE LIQUIDS
INTO SINTERED MAGNESIA COMPACTS

Contents

		Page
ABSTRACT		v
I.	INTRODUCTION	1
II.	THEORY OF CAPILLARY PENETRATION	3
	A. Basic Assumptions	3
	B. Physical Aspects of Capillary Penetration	4
	C. Chemical Aspects of Capillary Penetration	19
III.	THEORY OF PHASE DISTRIBUTION IN SOLID-LIQUID SYSTEMS	27
	A. The Derivation of Dihedral Angle Equation	27
	B. Phase Distribution in the Presence of Chemical Reactions in the System	32
IV.	EXPERIMENTAL	35
	A. Preparation of Sintered Magnesia Compact	35
	B. Preparation of the "Powdered Silicate Liquid" Compositions	36
	C. Permeation Studies	36
V.	RESULTS AND DISCUSSIONS	39
	A. Permeation of Liquids	39
	B. Chemical Reaction Effects	45
	C. Microstructure Effects	51
VI.	CONCLUSIONS	69
	A. Permeation Studies	69
	B. Microstructure Effects	70

Page

APPENDIX I 72

APPENDIX II 74

ACKNOWLEDGMENTS 77

REFERENCES 78

FIGURE CAPTIONS 80

PERMEATION OF SILICATE LIQUIDS INTO SINTERED MAGNESIA COMPACTS

Boon Wong

Inorganic Materials Research Division, Lawrence Berkeley Laboratory
and Department of Materials Science and Engineering,
College of Engineering; University of California,
Berkeley, California 94720

August 1972

ABSTRACT

Fundamentals of permeation kinetics of a liquid into a porous solid compact and the corresponding microstructure changes in the solid due to the permeating liquid, either in the presence or absence of reactions, were studied from both theoretical and experimental viewpoints.

Equations for capillary penetration were developed based on Poiseuille's law for capillary flow and the generalized thermodynamic concept of wetting of a solid by a liquid. Dihedral angle equation used for describing phase distribution (microstructure) in a solid-liquid system was thermodynamically derived and generalized.

Experimental studies were performed on the permeation of a number of silicate liquids into sintered magnesia (MgO) compacts of about 92.5% theoretical density. The experimental results support the theoretical predictions.

Permeation rate of a viscous liquid into a "homogeneous" compact with five capillaries depends mainly on the driving force for wetting, which in turn depends markedly on the presence and rate of any interfacial chemical reactions. In addition, the average permeation distance of the viscous liquid into the compact increases parabolically with time during

the initial stages. A negative deviation from this parabolic relationship usually results at later stages when the back-pressure developed by compression of entrapped gases becomes significant.

The microstructure of a relatively dense solid compact is markedly affected by a permeating liquid. The degree of material redistribution in the solid by a solution-precipitation process is significantly dependent on the degree of reactivity of the liquid with the solid.

I. INTRODUCTION

Permeation is a fundamental process in many branches of science and engineering. In the case of the behavior of refractory materials, studies have led to the conclusion that permeation plays an important role in the slag attack of refractories and on microstructure development.

Permeation of slags into refractories usually results in reactions and corrosion. During the past few years, the mechanism of slag attack on basic refractories of oxygen furnaces has been studied by several investigators. Herron, Beecham and Padfield[1] studied the attack of tar-impregnated magnesite brick by slags containing numerous oxides. They concluded that there were three main considerations in slag attack: (1) dependence of permeation of the slag into the brick structure on wetting of carbon by liquid slag, (2) permeation of the slag into the brick structure due to decarburization caused by reaction of carbon with some oxides in the slag, and (3) dissolution of MgO from the bulk of the brick by the slag. Later, Hodson and Richardson[2] studied the slag attack of dolomite, of fusion cast magnesite-chrome and of tar-impregnated magnesite. Basically, their results were similar to those obtained by Herron et al. With fusion cast magnesite-chrome, they further observed that slags rich in dicalcium ferrite caused greater attack than silicates since dicalcium ferrite dissolved intergranular spinel. Recently, Raju, Aksay and Pask[3] studied the permeation of silicates in magnesia and forsterite compacts. They observed that permeation occurred only when the solid was wet by the liquid and when open channels were available. When the solid reacted with the liquid, the formation of a saturated solid solution or equilibrium compound resulted in the blocking off of

the open channels at the macroscopic solid-liquid interface, preventing the permeation of silicates.

Once slag has permeated into the refractory structure, some redistribution of material occurs. Smith[4] first established the principle of equilibrium dihedral angles to explain the phase distributions (microstructures) of metallic alloy systems. He pointed out that the equilibrium dihedral angles is governed by the magnitudes of the grain boundary interfacial tension and solid-liquid interfacial tension. During the past ten years, White and his associates[5,6,7] studied systems based on mixtures of 85 wt% periclase and 15 wt% monticellite which consisted of a solid and liquid at 1550°C. With an addition of Cr_2O_3, they found that the degree of direct bonding between the magnesia grains was promoted, equilibrium dihedral angles was increased, and firing shrinkage and growth of pericalse grains were inhibited. In contrast to Cr_2O_3, additions of Fe_2O_3, Al_2O_3 and TiO_2 decreased the degree of direct bonding and the dihedral angle, and increased the firing shrinkage and grain growth. The equilibrium dihedral angle was found to be independent of the amount of liquid. The grain growth was found to be proportional to the one-third power of firing time.

The objective of this study was to understand, both from theoretical and experimental viewpoints, the fundamentals of permeation in the absence and presence of chemical reactions. The corresponding changes in some of the microstructures were also investigated.

II. THEORY OF CAPILLARY PENETRATION

In the following development of the theory of capillary penetration, two main types of capillaries shall be considered: (1) capillaries with flow from one end and the other end open to the atmosphere, and (2) capillaries with flow from one end and the other end isolated from the atmosphere. In order to simplify the problem, some basic assumptions are made.

A. Basic Assumptions

For laminar flow in a single uniform cylindrical capillary, Poiseuille's law (Appendix I) applies:

$$Q = \frac{dV}{dt} = \frac{\pi \Sigma P}{8\eta l_t} r^4$$

or

$$dV = \frac{\pi \Sigma P}{8\eta l_t} r^4 \, dt \qquad (1)$$

where

Q = discharge rate: volume of liquid penetrated per unit time

ΣP = algebraic sum of effective pressures that force the liquid along the capillary

V = volume of liquid penetrated

η = coefficient of viscosity of the liquid

l_t = length of the column of the liquid in the capillary at time t

r = radius of the cylindrical capillary.

The volume of the liquid in the capillary at time t can be given by

$$V = \pi r^2 l_t. \tag{2}$$

B. Physical Aspects of Capillary Penetration

In the absence of any chemical changes, the radius of the capillary can be treated as a constant. Differentiation of Eq. (2) gives

$$dV = \pi r^2 dl_t. \tag{3}$$

Substitution of Eq. (3) into Eq. (1) results in

$$\pi r^2 dl_t = \frac{\pi \Sigma P}{8\eta l_t} r^4 dt$$

or

$$\frac{dl_t}{dt} = \frac{\Sigma P}{8\eta l_t} r^2. \tag{4}$$

Equation (4) is then the general penetration rate equation in the absence of any chemical changes as the s-l (solid-liquid), and s-v (solid-vapor) interfaces of the system. It was first derived by Washburn.[8]

1. Consideration of the Parameters in the Rate Equation (Eq. (4))

a. The algebraic sum of the effective pressure components, ΣP. The components making up the effective pressure can be expressed as:

$$\Sigma P = P_A + P_h + P_c - P_i \tag{5}$$

where P_A = atmospheric pressure = 1 atmos. (in air)

P_h = hydraulic pressure = ρgh (ρ is the density of the liquid, g is gravitational constant, h is the depth of liquid above the center of the mouth of the capillary considered)

P_c = capillary pressure

P_i = internal back pressure caused by entrapped gas.

According to Laplace's equation for a spherical bubble

$$P_c = \frac{2\gamma_{lv}}{R} \tag{6}$$

where

γ_{lv} = surface tension at liquid-vapor interface

R = radius of the spherical bubble.

If complete wetting of the solid by the liquid, or spreading, does not exist, there is a contact angle θ.

In Figure 1, $\psi = 2(\frac{\pi}{2} - \theta)$

and

$$\sin \frac{\psi}{2} = \frac{r}{R}.$$

Then

$$\sin (\frac{\pi}{2} - \theta) = \frac{r}{R}$$

and also

$$\cos \theta = \frac{r}{R}$$

or

$$\frac{1}{R} = \frac{\cos \theta}{r} \tag{7}$$

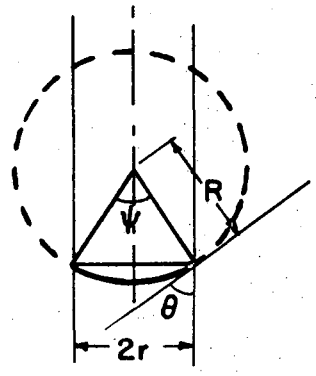

Figure 1

XBL 726-6352

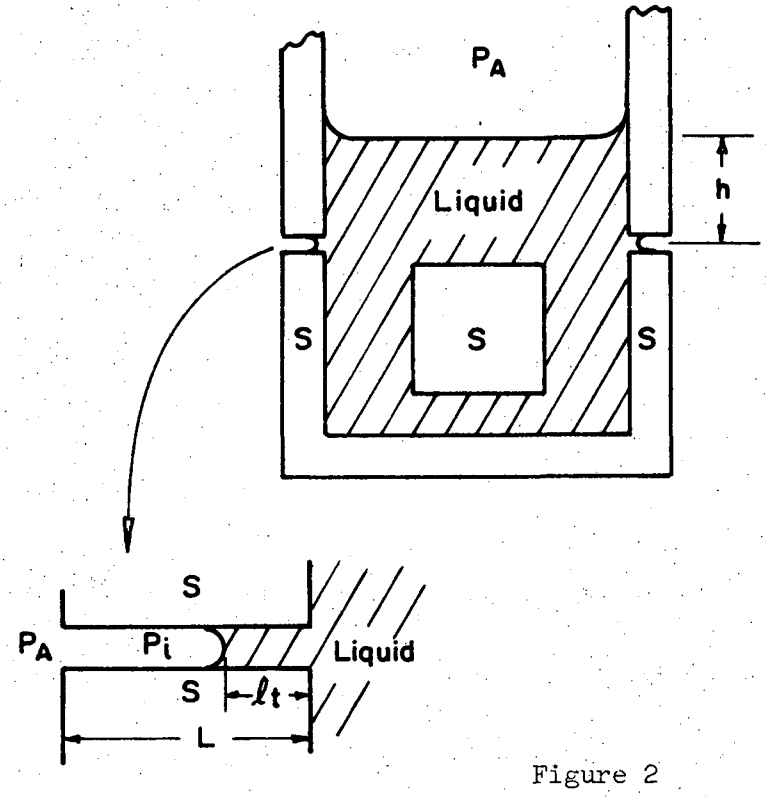

Figure 2

XBL726 -6353

Substitution of Eq. (7) into Eq. (6) gives

$$P_c = \frac{2\gamma_{lv} \cos \theta}{r} . \tag{8}$$

This is the expression for capillary pressure used in Washburn's paper.[8]

Since the driving force for wetting is $(\gamma_{sv}-\gamma_{sl})$ and according to Young's equation

$$\gamma_{sv}-\gamma_{sl} = \gamma_{lv} \cos \theta \tag{9}$$

where γ_{sv}, γ_{sl} are the solid-vapor, and solid-liquid interfacial tensions, respectively. In order to take the cases of spreading into consideration also, the more correct expression for capillary pressure should therefore be written as

$$P_c = \frac{2(\gamma_{sv}-\gamma_{sl})}{r} . \tag{10}$$

b. The coefficient of viscosity, η. In the absence of any chemical changes at the interfaces of the system, the composition of the liquid is constant at constant temperature. Therefore, η can be treated as a constant.

2. Some Typical Capillary Penetration Systems

a. Flow from one end.

(1) With other end open to the atmosphere. P_i in this case is a constant and equal to P_o which can be approximated by assuming

$P_i = P_o \tilde{\sim} P_A$. ($P_o$ is the initial pressure of the gases in the capillary.) Then

$$\Sigma P = P_h + P_c. \tag{11}$$

(i) Horizontal case (Figure 2). A combination of Eqs. (4), (10) and (11) gives

$$\frac{dl_t}{dt} = \frac{r}{8\eta l_t}\left[\rho g h + \frac{2(\gamma_{sv}-\gamma_{sl})}{r}\right]. \tag{12}$$

Integration of Eq. (12) gives

$$l_t^2 = \frac{1}{4\eta}\left[\rho g h\, r^2 + 2(\gamma_{sv}-\gamma_{sl})r\right]t. \tag{13}$$

Equation (13) is parabolic. The penetration distance, l_t, will thus continuously increase parabolically with time; i.e., there is no end-point penetration distance assuming that the capillary is semi-infinite.

(ii) Vertical cases

(a) Downward flow (Figure 3). With this configuration

$$P_h = \rho g(h + l_t). \tag{14}$$

From Eqs. (4), (11) and (14)

$$\frac{dl_t}{dt} = \frac{r^2}{8\eta l_t}\left[\frac{2(\gamma_{sv}-\gamma_{sl})}{r} + \rho g(h + l_t)\right]. \tag{15}$$

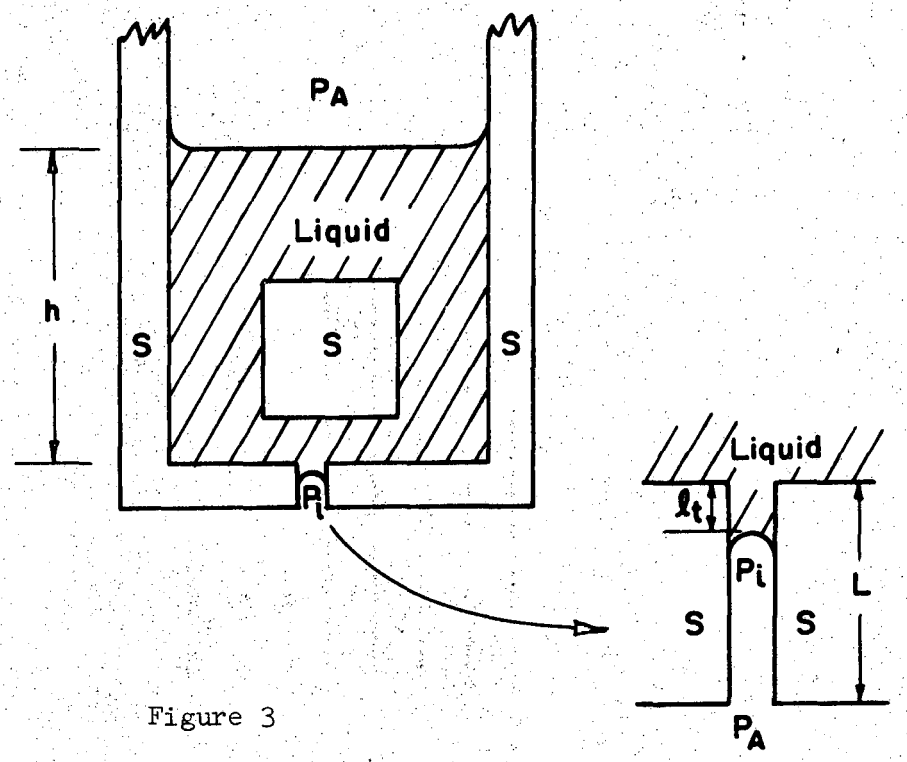

Figure 3

XBL 726-6354

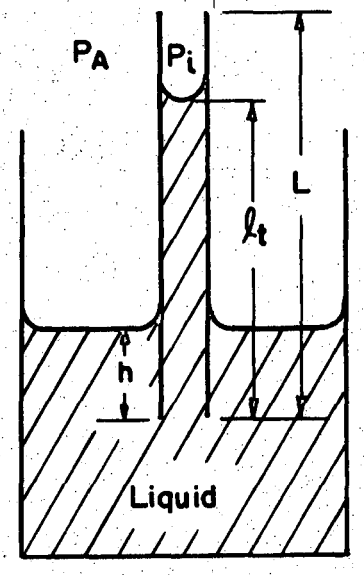

XBL 726-6355

Figure 4

Integration of Eq. (15) gives

$$t = \int_0^t dt = \frac{1}{r^2} \int_0^{l_t} \frac{8\eta l_t dl_t}{\left[\frac{2(\gamma_{sv}-\gamma_{sl})}{r} + \rho g(h+l_t)\right]} \quad . \tag{16}$$

Again, there is no end-point penetration distance.

b. Upward flow (Figure 4). In this case

$$P_h = \rho g(h-l_t). \tag{17}$$

From Eqs. (4), (11) and (17) it follows that

$$\frac{dl_t}{dt} = \frac{r^2}{8\eta l_t}\left[\frac{2(\gamma_{sv}-\gamma_{sl})}{r} + \rho g(h-l_t)\right] . \tag{18}$$

Integration of Eq. (18) gives

$$t = \int_0^t dt = \frac{1}{r^2} \int_0^{l_t} \frac{8\eta l_t dl_t}{\frac{2(\gamma_{sv}-\gamma_{sl})}{r} + \rho g(h-l_t)} \quad . \tag{19}$$

For vertical cases, when the firing time is very short, l_t is small and the hydraulic pressure effect is negligible. Under these conditions, the capillary penetration kinetic equation may be expressed approximately

as $l_t^2 = kt$ where k is an arbitrary constant. There is an end-point penetration distance for vertical upward flow case: setting Eq. (18) to zero gives

$$l_t\Big|_{t\to\infty} = \frac{2(\gamma_{sv}-\gamma_{sl})}{\rho g r} + h. \tag{20}$$

(2) With other end closed. The pressure P_i in the closed end of the capillary is

$$P_i = \frac{P_o \pi r^2 L}{\pi r^2 (L-l_t)} = \frac{P_o L}{(L-l_t)} \tag{21}$$

where L equals the total length of the capillary.

(i) Horizontal case (Figure 5). From Eqs. (4), (5) and (21) it follows that

$$\frac{dl_t}{dt} = \left[P_A + \rho g h + \frac{2(\gamma_{sv}-\gamma_{sl})}{r} - \frac{P_o L}{(L-l_t)}\right]\left[\frac{r^2}{8\eta l_t}\right]. \tag{22}$$

By letting $dl_t/dt = 0$ in Eq. (22), when steady state is reached, we obtain

$$\left[P_A + \rho g h + \frac{2(\gamma_{sv}-\gamma_{sl})}{r} - \frac{P_o L}{(L-l_t)}\right] = 0.$$

It follows that

$$l_t\Big|_{t\to\infty} = L\left[1 - \frac{P_o r}{P_A r + \rho g h r + 2(\gamma_{sv}-\gamma_{sl})}\right]. \tag{23}$$

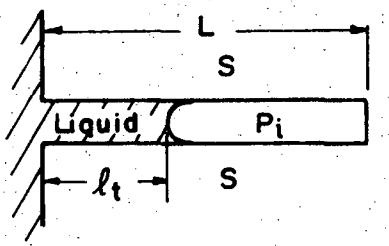

Figure 5. XBL 726-6356

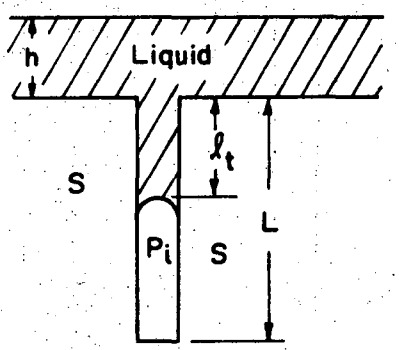

Figure 6. XBL 726-6357

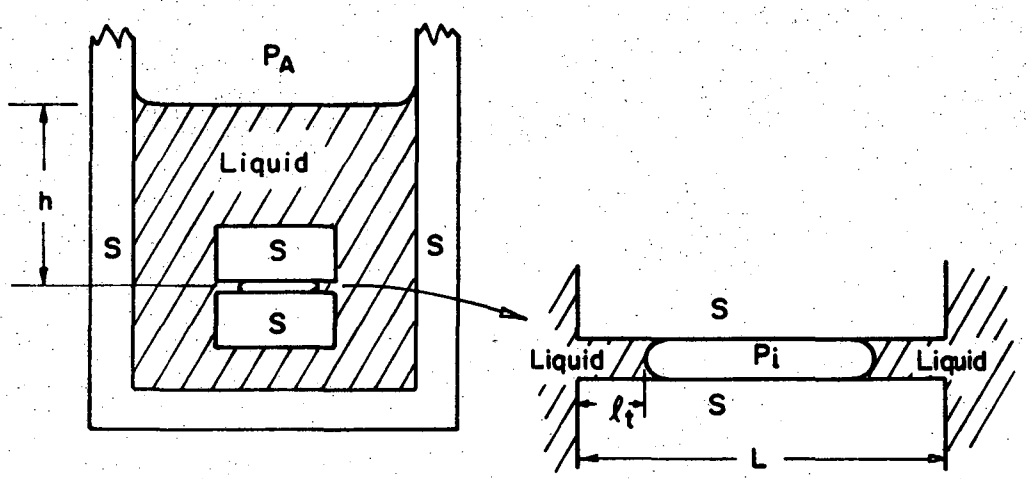

Figure 7. XBL 726-6358

From Eq. (23) it can be seen that in case of gas entrapment inside the capillary (assuming no solubility of gases in the liquid and no porosity leaks) l_t will never reach L; i.e. there is an end-point penetration distance again.

From Eq. (22), it follows that

$$t = \int_o^t dt = \frac{1}{r^2} \int_o^{l_t} \frac{8\eta l_t dl_t}{\left[P_A + \rho gh + \frac{2(\gamma_{sv}-\gamma_{sl})}{r} - \frac{P_o L}{(L-l_t)}\right]} \quad . \quad (24)$$

However, when t is small, l_t is also small and the back-pressure by compressed entrapped gases is thus negligible. Under these conditions, the capillary penetration kinetic equation may be expressed approximately as $l_t^2 = k_1 t$, where k_1 is an arbitrary constant.

(ii) Vertical cases

(a) Downward flow (Figure 6). From Eqs. (4), (5), (14) and (21) we find

$$\frac{dl_t}{dt} = \left[P_A + \rho g(h+l_t) + \frac{2(\gamma_{sv}-\gamma_{sl})}{r} - \frac{P_o L}{(L-l_t)}\right] \frac{r^2}{8\eta l_t} \quad . \quad (25)$$

Integration of Eq. (25) gives

$$t = \int_o^t dt = \frac{1}{r^2} \int_o^{l_t} \frac{8\eta l_t dl_t}{\left[P_A + \rho g(h+l_t) + \frac{2(\gamma_{sv}-\gamma_{sl})}{r} - \frac{P_o L}{(L-l_t)}\right]} \quad . \quad (26)$$

(b) Upward flow. From Eqs. (4), (5), (17) and (21) the differential is

$$\frac{dl_t}{dt} = \left[P_A + \rho g(h-l_t) + \frac{2(\gamma_{sv}-\gamma_{sl})}{r} - \frac{P_o L}{(L-l_t)} \right] \frac{r^2}{8\eta l_t} \tag{27}$$

Integration of Eq. (27) gives

$$t = \int_o^t dt = \frac{1}{r^2} \int_o^{l_t} \frac{8\eta l_t dl_t}{\left[P_A+\rho g(h-l_t) + \frac{2(\gamma_{sv}-\gamma_{sl})}{r} - \frac{P_o L}{(L-l_t)} \right]} . \tag{28}$$

When t is small, l_t is also small and the hydraulic pressure and the back-pressure of the compressed entrapped gases are negligible. Under these conditions, the capillary penetration kinetic equation may be expressed approximately as $l_t^2 = k_2 t$, where k_2 is an arbitrary constant. However, again there is an end-point penetration distance for each of the vertical cases with gas entrapment in the capillary.

b. Flow from Both Ends.

(1) Horizontal case (Figure 7). In this case

$$P_i = \frac{P_o L}{(L-2l_t)} \tag{29}$$

where L = the total length of the capillary. From Eqs. (4), (5) and (29) we have

$$\frac{dl_t}{dt} = \left[P_A + \rho gh + \frac{2(\gamma_{sv}-\gamma_{sl})}{r} - \frac{P_o L}{(L-2l_t)}\right]\left[\frac{r^2}{8\eta l_t}\right] \tag{30}$$

When $dl_t/dt = 0$, then Eq. (30) gives

$$l_t\Big|_{t\to\infty} = L\left[\frac{1}{2} - \frac{P_o r}{4(\gamma_{sv}-\gamma_{sl})+P_A r+\rho ghr}\right] \tag{31}$$

From Eq. (31), l_t will never reach the value $\frac{L}{2}$; i.e. there is again an end-point penetration distance.

Upon integration of Eq. (30) one finds

$$t = \int_o^t dt = \frac{1}{r^2}\int_o^{l_t} \frac{8\eta l_t dl_t}{\left[P_A+\rho gh + \frac{2(\gamma_{sv}-\gamma_{sl})}{r} - \frac{P_o L}{L-2l_t}\right]} \tag{32}$$

When t is small, l_t is also small and the back-pressure by compressed entrapped gases is negligible. Under these conditions, the capillary penetration kinetic equation may be expressed approximately as $l_t^2 = k_3 t$, where k_3 is an arbitrary constant.

(2) Vertical case

(i) Downward flow (Figure 8). In this case

$$P_h = \rho g(h_1+l_{1_t}) \tag{33}$$

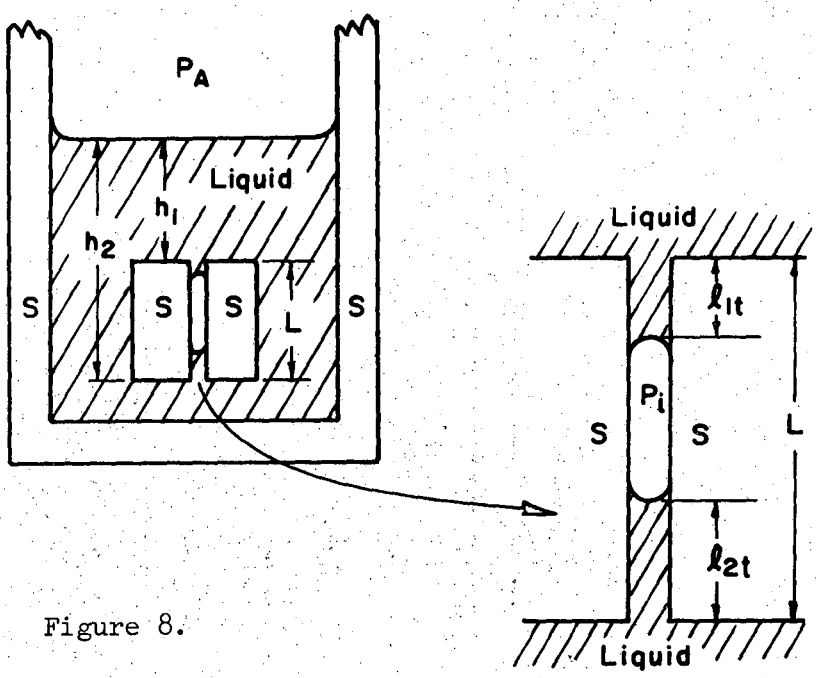

Figure 8.

XBL726-6359

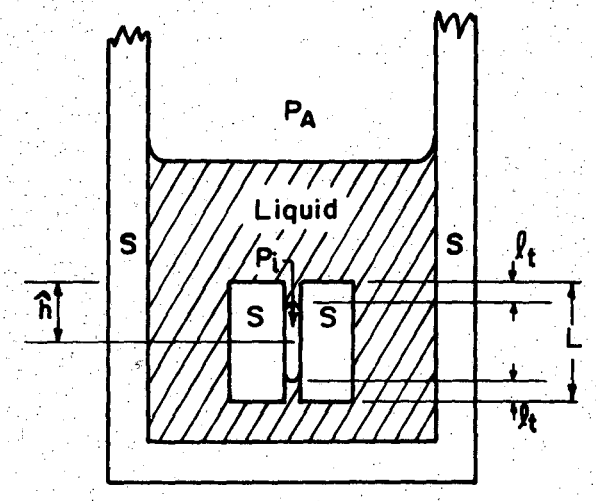

Figure 9.

XBL726-6360

and

$$P_i = \frac{P_o L}{L-(l_{1_t}+l_{2_t})} . \tag{34}$$

From Eqs. (4), (5), (33) and (34)

$$\frac{dl_{1t}}{dt} = \frac{r^2}{8\eta l_{1_t}} \left[\frac{2(\gamma_{sv}-\gamma_{sl})}{r} + \rho g(h_1+l_{1_t})+P_A - \frac{P_o L}{L-(l_{1_t}+l_{2_t})} \right]. \tag{35}$$

Integration of Eq. (35) gives

$$t = \int_o^t dt = \frac{1}{r^2} \int_o^{l_{1_t}} \frac{8\eta l_{1_t} dl_{1_t}}{\left[\frac{2(\gamma_{sv}-\gamma_{sl})}{r} + \rho g(h_1+l_{1_t})+P_A - \frac{P_o L}{L-(l_{1_t}+l_{2_t})} \right]} . \tag{36}$$

(ii) Upward flow (Figure 8). In this case

$$P_h = \rho g(h_2-l_{2_t}). \tag{37}$$

From Eqs. (4), (5), (34) and (37)

$$\frac{dl_{2_t}}{dt} = \left[\frac{2(\gamma_{sv}-\gamma_{sl})}{r} + \rho g(h_2-l_{2_t}) + P_A - \frac{P_o L}{L-(l_{1_t}+l_{2_t})} \right] \left[\frac{r^2}{8\eta l_{2_t}} \right]. \tag{38}$$

Integration of Eq. (38) gives

$$t = \int_o^t dt = \frac{1}{r^2} \int_o^{l_t} \frac{8\eta l_{2_t} dl_{2_t}}{\left[\frac{2(\gamma_{sv}-\gamma_{sl})}{r} + \rho g(h_2 - l_{2_t}) + P_A - \frac{P_o L}{L-(l_{1_t}+l_{2_t})}\right]} \quad (39)$$

When t is small, l_{1_t} and l_{2_t} are very small and the hydraulic pressure and the back-pressure by compressed entrapped gases are negligible. Under these conditions, the capillary penetration kinetic equations can be expressed approximately as $l_{1t}^2 = k_4 t$ and $l_{2t}^2 = k_5 t$; k_4, k_5 are arbitrary constants. However, with entrapment of gases in the capillary, an end-point penetration distance will exist for each of the vertical cases.

(iii) Average vertical flow (Figure 9). If $P_{\tilde{h}}$ is the average hydraulic pressure, then $P_{\tilde{h}} = \rho g \tilde{h}$, and the downward and upward flows are considered to be equally fast. Then

$$\frac{dl_t}{dt} = \left[P_A + \rho g \tilde{h} + \frac{2(\gamma_{sv}-\gamma_{sl})}{r} - \frac{P_o L}{L-2l_t}\right]\left[\frac{r^2}{8\eta l_t}\right] \quad (29a)$$

and

$$l_t\Big|_{t\to\infty} = L\left[\frac{1}{2} - \frac{P_o r}{4(\gamma_{sv}-\gamma_{sl}) + P_A r + \rho g \tilde{h} r}\right] . \quad (30a)$$

With entrapment of gases in the capillary, and end-point penetration distance will exist. Integration of Eq. (29a) gives

$$t = \int_0^t dt = \frac{1}{r^2} \int_0^{l_t} \frac{8\eta l_t dl_t}{\left[P_A + \rho g \tilde{h} + \frac{2(\gamma_{sv}-\gamma_{sl})}{r} - \frac{P_o L}{L-2l_t}\right]} \quad (31a)$$

When t is small, l_t is also small and hydraulic pressure and back-pressure by compressed entrapped gases are negligible. Again under these conditions, the capillary penetration kinetic equation may be expressed approximately as $l_t^2 = k_6 t$, where k_6 is an arbitrary constant.

C. Chemical Aspects of Capillary Penetration

In this section, only the horizontal penetration cases are taken into consideration. For the cases of vertical penetration, analogous treatments can be applied similar to those in Section II-B-2.

1. Physical Wetting

The wetting process of a solid by a liquid, in brief, is that process during which the solid-vapor interfacial area is replaced by a solid-liquid interfacial area. Usually the degree of wetting is indicated by the contact angle θ as shown in Fig. 10. At equilibrium, if $0° \leqslant \theta < 90°$, wetting is said to occur. Complete wetting or spreading develops when the driving force for wetting is greater than γ_{lv}, corresponding to $\theta \leqslant 0°$. If $90° < \theta \leqslant 180°$ non-wetting of the solid exists.

Young's equation, Eq. (9), however, has its restrictions. Referring to Fig. 11, it is only applicable for those conditions where both $0° \leqslant \theta \leqslant 180°$ $(1 \leqslant \cos\theta \leqslant -1)$ and $|\gamma_{sv}-\gamma_{sl}| \leqslant \gamma_{lv}$. When γ_{sl} is large enough

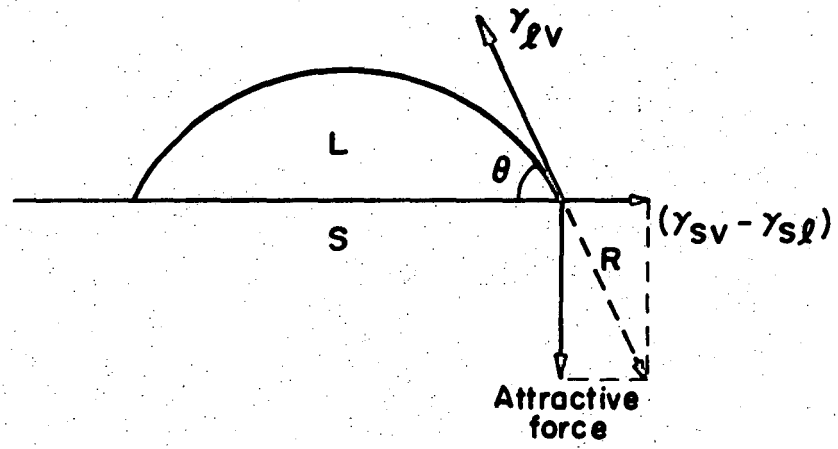

Figure 10.

XBL 726-6361

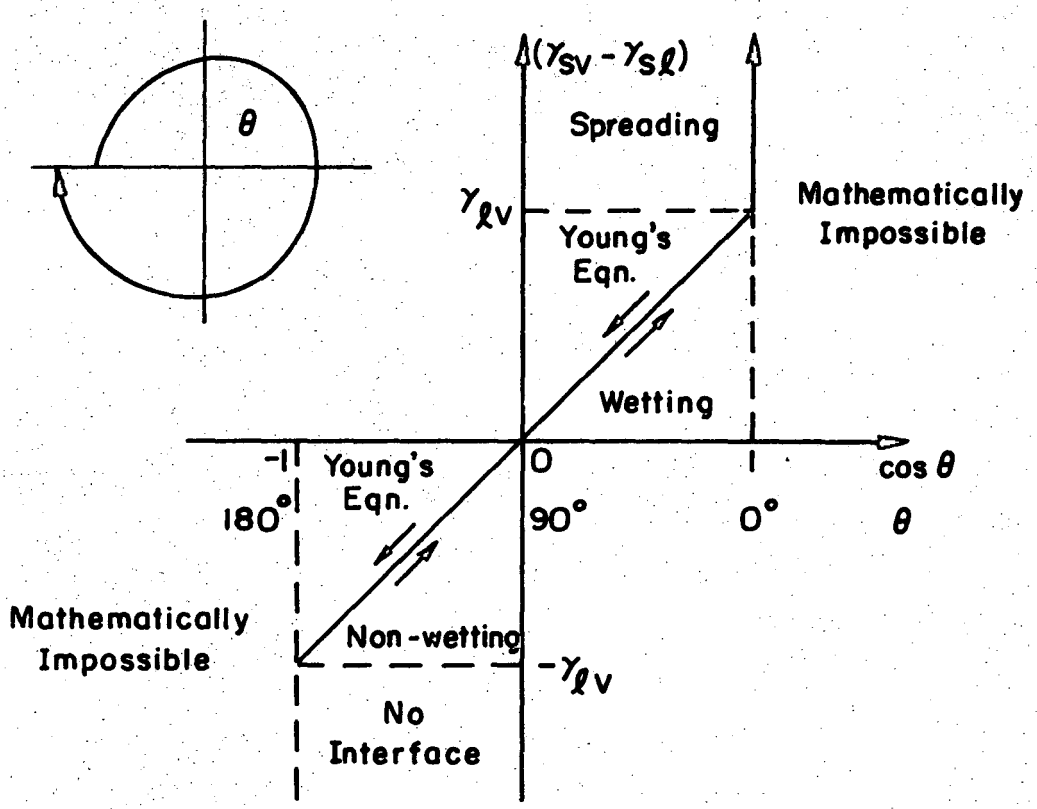

Figure 11.

XBL 726-6362

to make $\gamma_{sv}-\gamma_{sl} > -\gamma_{lv}$, then no interface forms. The only condition which is of particular importance in studies on wetting that cannot be described by Young's equation is the condition $\gamma_{sv}-\gamma_{sl} > \gamma_{lv}$, i.e. spreading. A discussion follows.

2. Effect of Chemical Factors on Wetting

In the firing of refractories chemical changes frequently occur at solid-liquid interfaces. The degree of wetting of the solid by the liquid is then improved, and the contact angle decreases or spreading occurs.

Young's equation, as can be understood from its form, only applies to steady state cases. Therefore, in the presence of chemical reactions at interfaces, Young's equation cannot be applied directly. A modified form of Young's equation should then be developed.[9]

If f_{sv}, f_{sl}, f_{lv} = specific surface free energies at solid-vapor, solid-liquid and liquid-vapor interfaces, respectively

μ_i = chemical potential of component i

Γ_i^{sv}, Γ_i^{sl}, Γ_i^{lv} = excess interfacial concentrations of the i^{th} component in a system at the solid-vapor, solid-liquid and the liquid-vapor interfaces respectively over the concentration in the bulk.

$\sum_j \mu_j \Gamma_j^{sl}$ = surface free energy contribution at the s-l interface due to a s-l interface reaction. Then

$$\left[f_{sv} - \sum_i \mu_i \Gamma_i^{sv}\right] - \left[f_{sl} - \sum_i \mu_i \Gamma_i^{sl} + (*-\left|\sum_j \mu_j \Gamma_j^{sl}\right|)\right] \geq \left[(f_{lv} - \sum_i \mu_i \Gamma_i^{lv})\cos\theta\right]. \tag{40}$$

*"Minus" sign, since s-l interface reactions always lead to a lower free energy at s-l interface.[9]

The inequality occurs usually when the reaction term

$$|\sum_j \mu_j \Gamma_j^{sl}|$$

is large.

3. Kinetics of Wetting in Presence of Chemical Reactions

Chemical reactions between the solid and contacting liquid can markedly affect the wetting phenomenon. During the course of a reaction, the reaction term

$$|\sum_j \mu_j \Gamma_j^{sl}|$$

which contributes to the driving force for wetting, may markedly affect the wetting behavior. Thus, wetting will depend on the product ratio of the activities of the reactants in the solid and in the liquid at the solid-liquid-vapor junctions. With the configuration shown in Fig. 12, the following assumptions on the systems to be discussed are made: (a) diffusion of any reactant species A in a liquid is always fast, (b) dissolution rate of the source material AX of the reactant A in the liquid, $AX \rightarrow A+X$, is always fast, (c) the solid-liquid interface reaction $A+S \rightarrow AS$, is always fast, and (d) the liquid is always saturated with respect to the components of the solid.

The first case to be considered is one in which diffusion of species A in the solid is rate controlling. No depletion of reactants occur in the liquid and the solid (i.e. each one of the reactant species has an "unlimited" reservoir of its own source material so that each of them

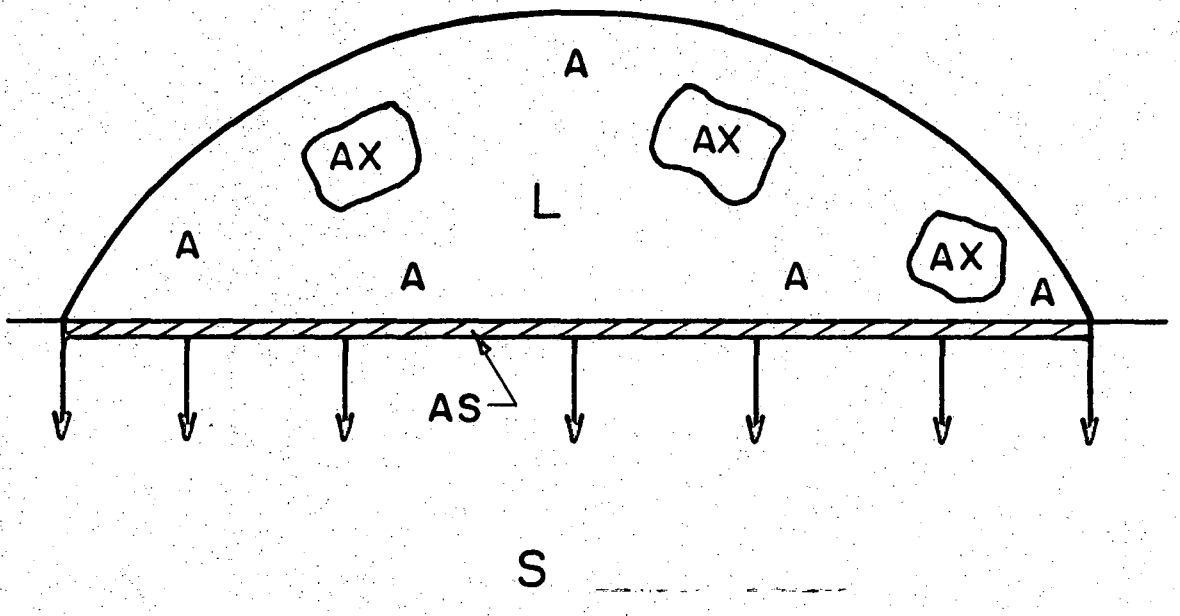

Figure 12.

XBL 728-6757

always can remain at maximum concentration or solubility limit in the liquid). Therefore, the ratio of the activity of species A in the solid and in the liquid at the solid-liquid-vapor junctions is very small; significant and rapid reaction always occurs at the three-phase junctions between the vapor, liquid and solid. The term

$$\left|\sum_j \mu_j \Gamma_j^{sl}\right|$$

is then always significant in Eq. (40). As a result, low or zero contact angles (good wetting or spreading) usually exist.

The second case is one in which either a depletion of the reactants in one of the phases occurs or when diffusion of species A in the solid is so fast that the diffusing species enters the solid beyond the periphery of the liquid drop. The significance of the reaction at the three-phase junctions will then be reduced (the ratio of the activity of species A in the solid and in the liquid at the three-phase junctions approaches one) and larger contact angles are usually observed.[10] Depletion of the reactants in the liquid usually leads to the "pulling back" of the liquid after reaching a low contact angles or spreading but not both in the initial stages of reaction. Fast diffusion rate of species A in the solid usually saturates the area of the solid to be wetted ahead of the liquid part, resulting in an "equilibrium" contact angle. Under these cases, the reaction term vanishes and Eq. (40) may be written in the following steady state form:

$$\left[f_{sv} - \sum_i \mu_i \Gamma_i^{sv}\right] - \left[f_{sl} - \sum_i \mu_i \Gamma_i^{sl}\right] = \left[\left(f_{lv} - \sum_i \mu_i \Gamma_i^{lv}\right) \cos \theta\right]. \qquad (41)$$

4. Capillary Penetration in the Presence of Chemical Reactions

If it is assumed that (a) the change in viscosity of the liquid is negligible, (b) the capillary radius is constant, and (c) the dominant pressure acting at the liquid head is the capillary pressure of wetting, the penetration rate of a liquid into a capillary then depends on the wetting behavior of the liquid which in turn depends greatly on the chemical reactivity of the liquid with the solid.

In the presence of chemical reactions, Eq. (10) giving the capillary pressure of wetting can be written in a more general way as

$$P_c = \frac{2\left\{\left[f_{sv} - \sum_i \mu_i \Gamma_i^{sv}\right] - \left[f_{sl} - \sum_i \mu_i \Gamma_i^{sl} + \left(-\left|\sum_j \mu_j \Gamma_j^{sl}\right|\right)\right]\right\}}{r} \qquad (42)$$

Following the previous relationships, if a reaction occurs that contributes to increasing the capillary pressure and is sustained, the rates of penetration of such liquids are enhanced. In the absence of the term

$$\left|\sum_j \mu_j \Gamma_j^{sl}\right|$$

as a contributing factor to the capillary pressures as described

previously, the rates of penetration of the liquids are slower with all other conditions being the same.

In case of no significant back-pressure introduced by the presence of compressed entrapped gases in the capillary, the penetration equation can be written in a general and simple way as:

$$\frac{dl_t}{dt} = \frac{r}{4\eta l_t} \left\{\left[f_{sv} - \sum_i \mu_i \Gamma_i^{sv}\right] - \left[f_{sl} - \sum_i \mu_i \Gamma_i^{sl} + \left(- \left|\sum_j \mu_j \Gamma_j^{sl}\right|\right)\right]\right\}$$

or upon integration

$$\frac{l_t^2}{t} = \frac{r}{2\eta} \left\{\left[f_{sv} - \sum_i \mu_i \Gamma_i^{sv}\right] - \left[f_{sl} - \sum_i \mu_i \Gamma_i^{sl} + \left(- \left|\sum_j \mu_j \Gamma_j^{sl}\right|\right)\right]\right\} \qquad (43)$$

Equation (43) is parabolic. Therefore, whenever capillary pressure is dominant, the kinetic equation for capillary penetration can be expressed approximately as $\ell_t^2 = K_6 t$, where K_6 is an arbitrary constant.

III. THEORY OF PHASE DISTRIBUTION IN SOLID-LIQUID SYSTEMS

Once a liquid has permeated into the solid compact along open channels, redistribution of the solid phase may occur. First, the spatial arrangement of the phases in equilibrium structures, as has been described for alloys,[4] can be accounted for in terms of surface tension balances at intersections of interfaces as shown in Fig. 13 and represented by

$$\gamma_{ss} = 2\gamma_{sl} \cos \frac{\phi}{2} \tag{44}$$

where

γ_{ss} = interfacial tension in solid grain boundary.

γ_{sl} = interfacial tension in the solid-liquid interface.

ϕ = dihedral angle between solid-liquid interfaces measured in the liquid phase at the junction of the liquid with the grain boundary.

A. The Derivation of Dihedral Angle Equation

The following derivation of the dihedral angle equation (Eq. (43)) for ϕ is based on the model given by White.[11] The assumptions are that there are two phases (one solid and one liquid), and that the solid particles are spheres of equal size initially in contact and enveloped by the liquid phase.

At constant temperature, pressure and composition, a solid-liquid system such as the one shown in Fig. 14 gives:

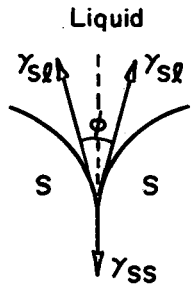

Figure 13. XBL726-6368

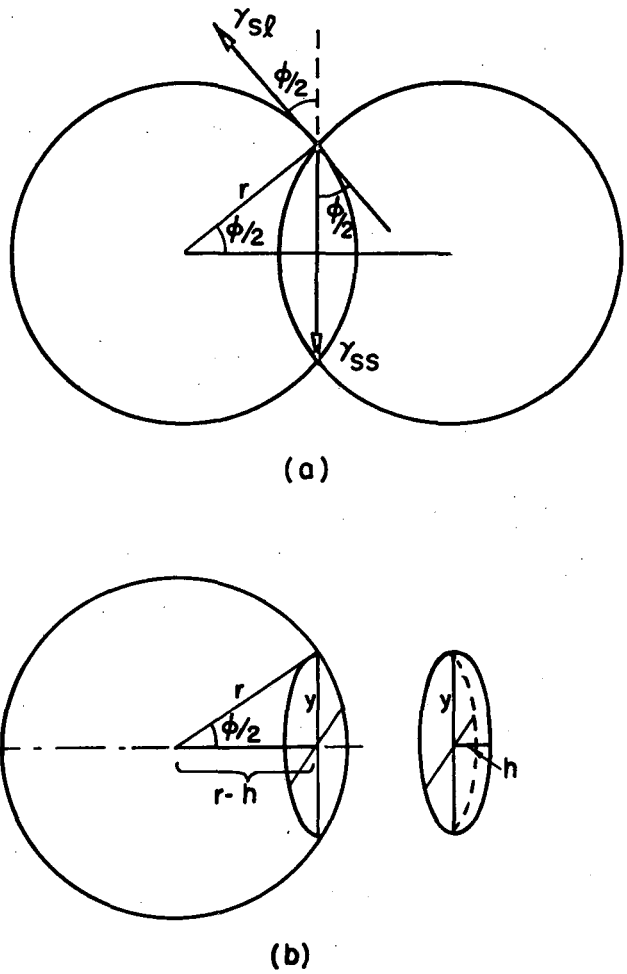

Figure 14. XBL726-6369

$$(\delta G)_{sy} = \delta \int_{A} \gamma dA = \delta \int_{A_{ss}} \gamma_{ss} dA_{ss} + \delta \int_{A_{sl}} \gamma_{sl} dA_{sl} \tag{45}$$

where $(\delta G)_{sy}$ = differential change of Gibbs free energy for the entire system

γ = surface tension

A = interfacial area

During liquid phase sintering, the interpenetration of the two spherical particles occurs. The material of the caps displaced is assumed to be distributed uniformly over the spherical surfaces by a solution and re-precipitation process. Then the material balance for each spherical particle requires that

$$\rho V_i = \rho(V_t - V_{cap}) \tag{46}$$

where

V_i = initial volume of each spherical particle

V_t = volume of each interpenetrating spherical particle

V_{cap} = volume of the cap removed from each particle

ρ = the density of the solid.

Differentiation of Eq. (46) results in $dV_t - dV_{cap} = 0$ or

$$4r^2dr - 2rhdh - h^2dr + h^2dh = 0$$

$$(4r^2 - h^2)\, dr = (2rh - h^2)dh$$

$$dr = \frac{h(2r - h)}{(2r + h)\,(2r - h)}\, dh$$

$$dr = \left(\frac{hdh}{2r + h}\right) \tag{47}$$

where r is the radius of the spherical particle with a volume V_t and h is the height of the cap.

Let A = the surface area of each spherical particle with a volume V_t, A_1 = the curved surface area of the cap, and A_2 = the base area of the cap, then

$$A = 4\pi r^2 \tag{48}$$

$$A_1 = 2\pi rh \tag{49}$$

$$A_2 = \pi y^2 = \pi[r^2 - (r-h)^2] = \pi[2rh-h^2]. \tag{50}$$

Differentiation of Eqs. (48), (49) and (50) results in

$$dA = 8\pi r dr \tag{51}$$

$$dA_1 = 2\pi r dh + 2\pi h dr \tag{52}$$

$$dA_2 = 2\pi r dh + 2\pi h dr - 2\pi h dh. \tag{53}$$

From Eq. (45),

$$(\delta G)_{\text{one sphere}} = \delta \int_{A_{ss}=A_2} \frac{\gamma_{ss}}{*2}\, dA_2 + \delta \int_{A_{sl}=A-A_1} \gamma_{sl}(dA-dA_1) \tag{54}$$

Substituting Eqs. (51), (52) and (53) into Eq. (54) one finds

$$(\delta G)_{\text{one sphere}} = \pi\left[-\delta\int\gamma_{ss}(hdh-hdr-rdh) + 2\delta\int\gamma_{sl}(4rdr-rdh-hdr)\right]. \tag{55}$$

Substituting Eq. (47) into (55), one obtains

$$(\delta G)_{\text{one sphere}} = \pi\left[\begin{array}{l} -\delta\int\dfrac{\gamma_{ss}(rhdh-2r^2dh)}{2r+h} \\ \\ +\ 2\ \delta\int\dfrac{\gamma_{sl}(3rhdh-2r^2dh-h^2dh)}{2r+h} \end{array}\right]. \tag{56}$$

*Divided by 2 because each base of the cap is assumed to be equally shared by 2 spheres.

At equilibrium, $(\delta G)_{\text{one sphere}} = 0$. Equation (56) becomes

$$\frac{\gamma_{ss}}{2\gamma_{sl}} = -\frac{(2r-h)(r-h)}{r(h-2r)} = \frac{r-h}{r} = \cos\frac{\phi}{2}$$

or

$$\gamma_{ss} = 2\gamma_{sl}\cos\frac{\phi}{2}\,. \tag{44}$$

When $\gamma_{ss} \geqslant 2\gamma_{sl}$, $\phi = 0$ and complete penetration of the liquid phase between the two solid grains will occur. When $\gamma_{ss} < 2\gamma_{sl}$, ϕ will have a finite value and the liquid cannot penetrate completely along the grain boundary. The degree of penetration will decrease as the ratio $\frac{\gamma_{ss}}{\gamma_{sl}}$ decreases and ϕ increases. When $\gamma_{ss} = \gamma_{sl}$, the solid and liquid behave as identical phases and all three angles between the intersecting boundaries will be equal ($\phi = 120°$). If $\gamma_{ss} < \gamma_{sl}$, then $120° < \phi \leqslant 180°$. Therefore, a liquid will penetrate the grain boundaries only when $\gamma_{ss} \geqslant 2\gamma_{sl}$.

B. Phase Distribution in the Presence of Chemical Reactions in the System

Chemical reactions do play an equally significant role in the development of microstructures in solid-liquid systems as in the wetting behavior of different liquids on solids. When reactions occur in a solid-liquid system, analogous to Young's equation, the dihedral angle equation for describing the phase distribution should be written in a more general form as follows:

$$\left[f_{ss} - \sum_i \mu_i \Gamma_i^{ss}\right] = 2\left[\left(f_{sl} - \sum_i \mu_i \Gamma_i^{sl}\right) + \left(*- \left|\sum_j \mu_j \Gamma_j^{sl}\right|\right)\right] \cos\frac{\phi}{2} \qquad (57)$$

where

f_{ss} = specific surface free energy at solid-solid interface

$\sum_i \mu_i \Gamma_i^{ss}$ = specific surface free energy change due to composition change at solid-solid interface, and the other terms are defined the same as before.

Using the same basic assumptions as those made in the theoretical development of capillary penetration, two frequently observed cases in phase distributions due to occurrence of chemical reactions can then be classified.

In the first case, the diffusion of the reaction product species into the solid is assumed to be slow. Then, the term $\left|\sum_j \mu_j \Gamma_j^{sl}\right|$ in Eq. (57) is significant in the initial stages. Therefore, the dihedral angle will usually be low or zero and the liquid has a chance to penetrate most of the grain boundaries. If the reaction involves some solution of the solid which would occur readily at grain boundaries, then penetration of the grain boundaries would be enhanced. When the reactions become completed and the system approaches thermodynamic equilibrium, the dihedral angle and grain-grain contacts will increase.

In the second case the diffusion of the reaction product species into the solid is assumed to be fast relative to the s-l interface reactions. Under these conditions, the liquid will come in contact with solid that is essentially in equilibrium with the liquid. As a result,

*See footnote on page 21.

the term $\left|\sum_j \mu_j \Gamma_j^{sl}\right|$ vanishes and penetration along existing grain boundaries will not occur. Equation (57) may then be written in the following steady state form:

$$\left[f_{ss} - \sum_i \mu_i \Gamma_i^{ss}\right] = 2\left[\left(f_{sl} - \sum_i \mu_i \Gamma_i^{sl}\right)\right] \cos\frac{\phi}{2} \quad . \tag{57a}$$

IV. EXPERIMENTAL

Model permeation systems were set up to test and confirm the theories in Sections II and III. MgO powder was chosen to form compact. Ten "powdered silicate liquid" compositions containing various sesquioxides, having different chemical reactivities with MgO at the annealing temperature, were prepared as permeating liquids. These materials were chosen because of their importance in the basic refractory fabrication processes.

A. Preparation of Sintered Magnesia Compact

Reagent grade 99% pure magnesium oxide powder of Allied Chemical Corporation, N.Y.,* was isostatically pressed under 30,000 psi at room temperature forming a large compact approximately 3 cm in diameter and 7 to 9 cm in length. The pressed compact was slowly heated and sintered in air at 1500°C for 13 hours, and at 1550°C for 3 hours, and furnace-cooled to room temperature.

After sintering, the compact was cut into approximately equal-sized small specimens with dimensions roughly 0.54 cm x 0.54 cm x 0.63 cm and polished. The average bulk density of the compacts was about 3.31 gm/cc with an average open porosity 3.1%. Taking the theoretical density of pure MgO single crystals as 3.58 gm/cc,[12] the relative density for the compacts was 92.5% of theoretical density. The compacts were then stored in a desiccator until later use.

---

*Appendix II

B. Preparation of the "Powdered Silicate Liquid" Compositions

Ten different "powdered silicate liquid" compositions were prepared at room temperature by intimately dry mixing powders in tumblers for about 24 hours. Mixtures of fine powders of MgO, $CaCO_3$, SiO_2 with additions of the sesquioxides of Cr_2O_3, Fe_2O_3 and Al_2O_3* were prepared whose compositions after reaction and melting were:

(1) $[CaO \cdot MgO \cdot SiO_2]$

(2) 99 wt% $[CaO \cdot MgO \cdot SiO_2]$ + 1 wt% $[Cr_2O_3]$

(3) 90 wt% $[CaO \cdot MgO \cdot SiO_2]$ + 10 wt% $[Cr_2O_3]$

(4) 85 wt% $[CaO \cdot MgO \cdot SiO_2]$ + 15 wt% $[Cr_2O_3]$

(5) 95 wt% $[CaO \cdot MgO \cdot SiO_2]$ + 5 wt% $[Fe_2O_3]$

(6) 55 wt% $[CaO \cdot MgO \cdot SiO_2]$ + 45 wt% $[Fe_2O_3]$

(7) 45 wt% $[CaO \cdot MgO \cdot SiO_2]$ + 55 wt% $[Fe_2O_3]$

(8) 99 wt% $[CaO \cdot MgO \cdot SiO_2]$ + 1 wt% $[Al_2O_3]$

(9) 90 wt% $[CaO \cdot MgO \cdot SiO_2]$ + 10 wt% $[Al_2O_3]$

(10) 85 wt% $[CaO \cdot MgO \cdot SiO_2]$ + 15 wt% $[Al_2O_3]$

No premelting of these compositions was made, and the tumbled mixtures were stored in a desiccator until later use. It was found that premelting was not necessary for the subsequent experiments.

C. Permeation Studies

Each "silicate liquid" powder mixture was packed tightly on top of a sintered magnesia compact specimen (with the polished surface up) in a magnesia** crucible of 0.76 cm in diameter. Then the crucible was placed in a Pt crucible which in turn was placed in an air atmosphere furnace

*Appendix II

**Norton Company, Magnorite-480 fused magnesia.

with $MoSi_2$ heating elements, shown in Fig. 15. The furnace, which was initially at about 1150°C to 1200°C, was then gradually heated up to 1550°C. Five assemblies of each composition were heated at 1550°C for periods of 5 minutes, 15 minutes, one-half hour, one hour, and two hours. All specimens were furnace-cooled to 1200°C and then quenched to room temperature in air.

Each specimen was cut vertically into equal halves. The cut sections were mounted in resin and were subjected to standard ceramographic polishing. Careful examinations under reflected light with magnifications ranging from 80X to 400X were subsequently made of each specimen.

Photographic studies on microstructures were done by using a metallographic microscope. A number of typical permeation specimens were etched in order to emphasize the grain boundaries and distribution of liquid phases in the magnesia compacts.

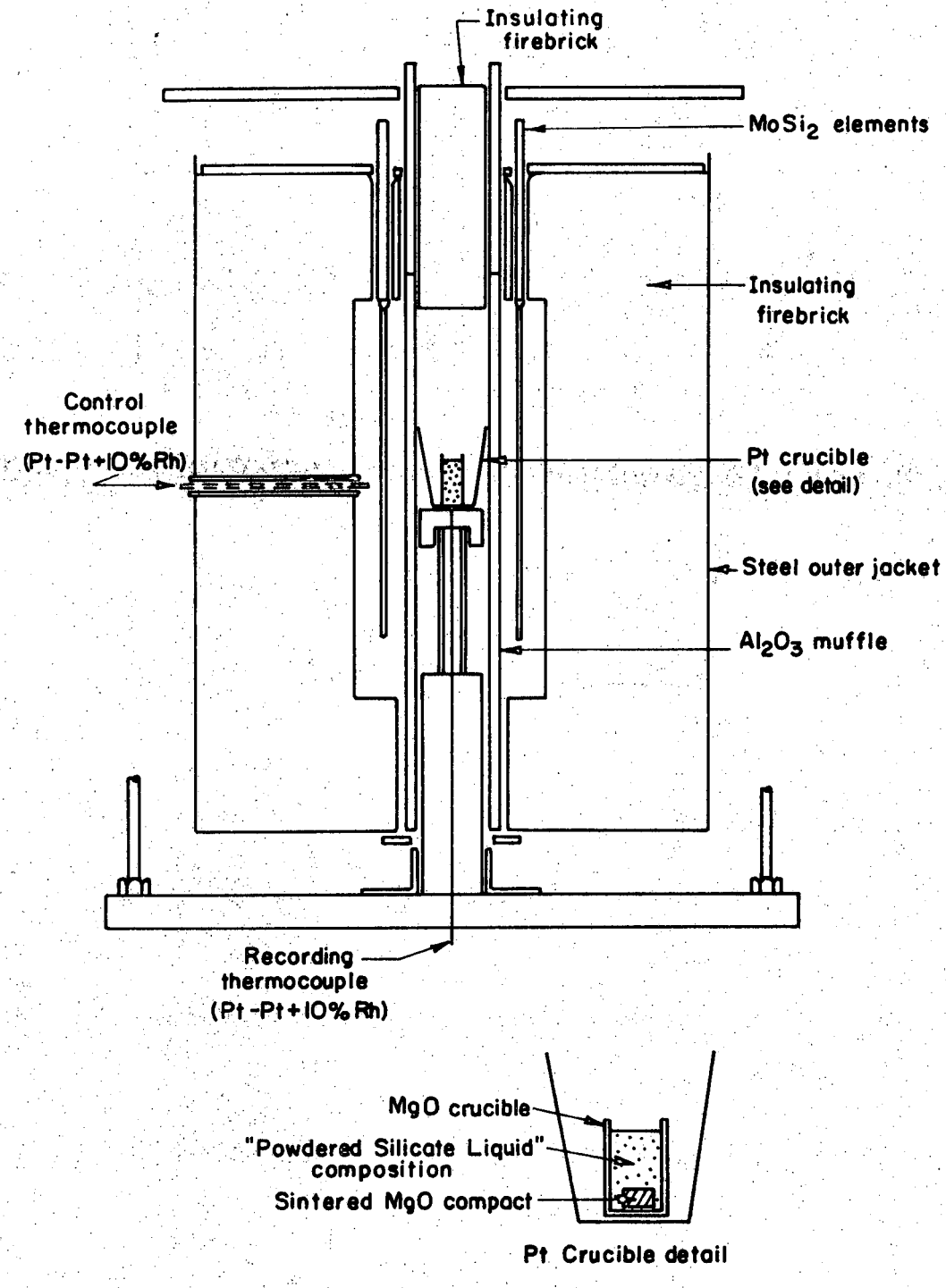
Insulating firebrick
$MoSi_2$ elements
Insulating firebrick
Control thermocouple (Pt-Pt+10%Rh)
Pt crucible (see detail)
Steel outer jacket
Al_2O_3 muffle
Recording thermocouple (Pt-Pt+10%Rh)
MgO crucible
"Powdered Silicate Liquid" composition
Sintered MgO compact
Pt Crucible detail
XBL 726-6363

Figure 15.

V. RESULTS AND DISCUSSIONS

A. Permeation of Liquids

A typical section of the microstructure of the MgO compacts used for permeation studies with 92.5% of the theoretical density is shown in Fig. 16. The available channels for permeation were very small and essentially along triple lines which appear as pores on triple points in the two-dimensional figure. As a result, difficulties were experienced in determining the permeation distance of the liquids into the MgO compacts. In addition, the non-homogeneous features of the microstructure, such as non-uniform distribution of pores and discontinuous grain growth, further complicated the determination of permeation distances into the compacts. Rigorous quantitative results were thus not attainable.

From the analyses in Section II, physical permeation (without any chemical reactions in the system) of a liquid into a porous solid should be different along horizontal and vertical directions because of different hydraulic pressure contributions. Monticellite ($CaO \cdot MgO \cdot SiO_2$ or CMS) liquid at 1550°C according to the phase diagram of Osborn and Muan[13] is at chemical equilibrium with MgO after precipitation of a small amount of MgO, probably on the magnesia grains. Figure 17 shows log-log relationships of permeation distance of this liquid and annealing time at 1550°C for average horizontal flow (Curve A), vertical downward flow (Curve B), and vertical upward flow (Curve C). The differences can be seen to be in accordance with theoretical predictions. Since these differences are small, however, equally significant results can be obtained by indicating the permeation of a given liquid either by averaging Curves A, B and C, which is shown as Curve D, or by directly using

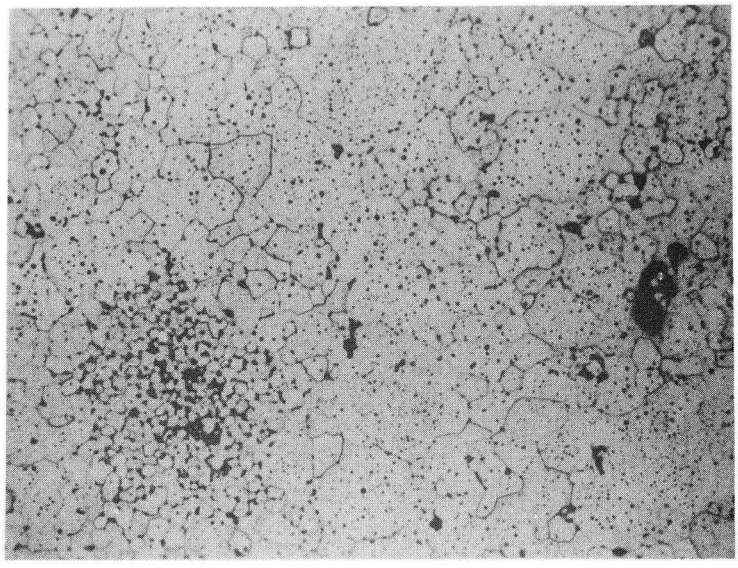

Figure 16a.

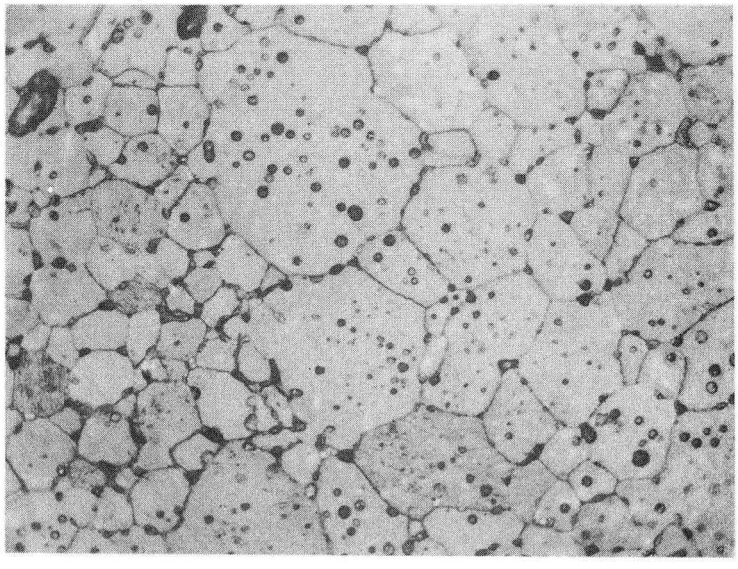

XBB-726-3053

Figure 16b.

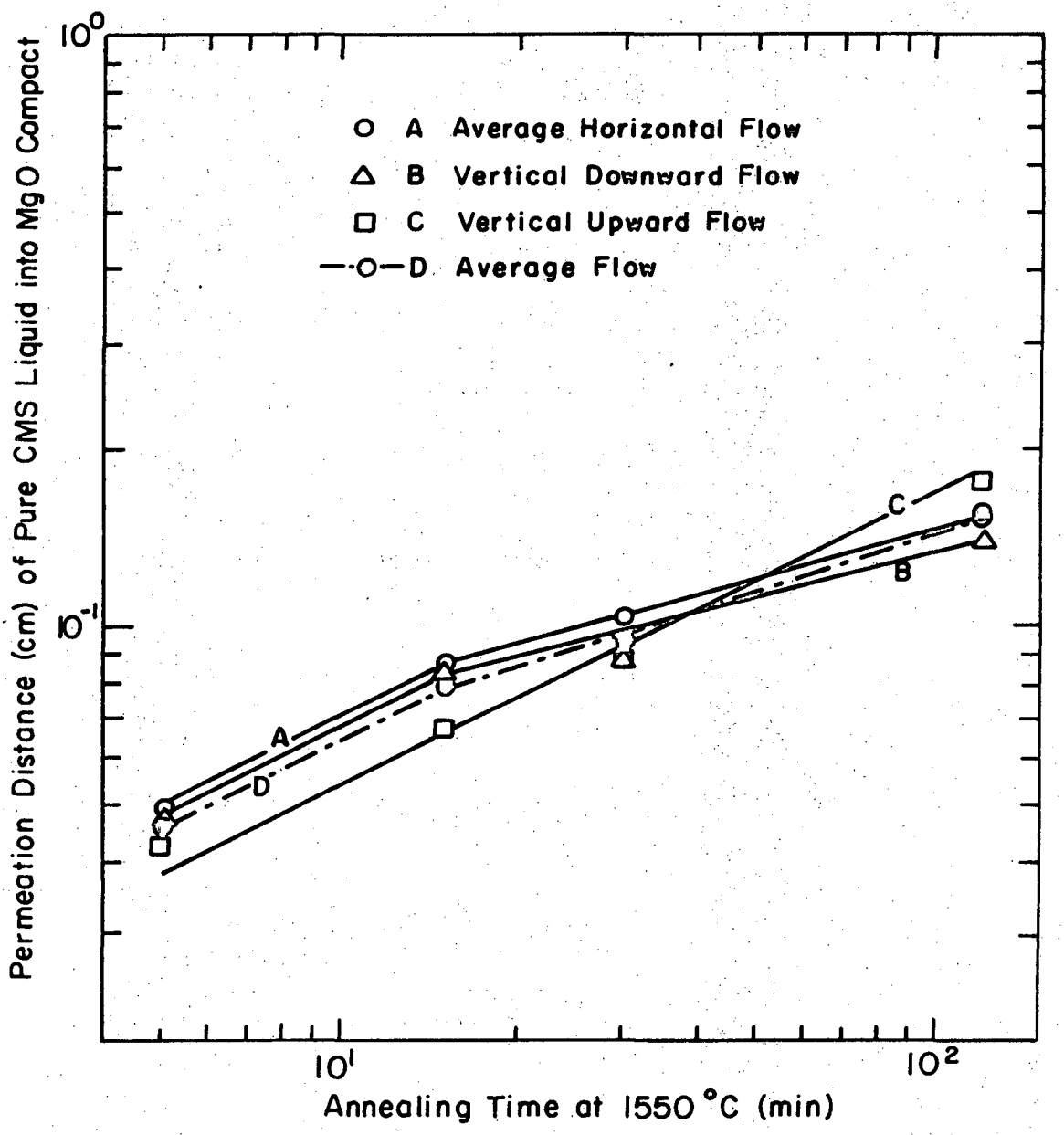

XBL726-6364

Figure 17.

Curve A which is based on a constant hydraulic pressure.

Figures 18 and 19 show the linear and logarithmic relationships of average horizontal permeation distances with time at 1550°C of the different experimental silicate liquids. The Cr_2O_3-containing liquids had the fastest permeation rates: the 15% and 10% Cr_2O_3 liquids completely permeated the MgO compact within 5 minutes at temperature, and 1% Cr_2O_3 liquid permeated through the compact after 15 minutes. The 5% Fe_2O_3 liquid was the fourth fastest, whereas no permeation occurred with the high Fe_2O_3 concentration liquids (45% and 55% Fe_2O_3). The 15%, 10% and 1% Al_2O_3-containing liquids were the fifth, sixth and seventh fastest, respectively. CMS liquid without any additives had the slowest permeation rate.

Figure 19 also shows that all of the curves in the initial stages of permeation have an average slope of approximately one-half, or that the permeation distance is proportional to the square root of time in accordance with Eq. (43). This relationship is maintained into the later stages of permeation except by the curves for the slower permeating liquids such as pure CMS and 1% Al_2O_3-containing liquid which show average slopes of less than one-half after longer times. When the permeation distance of the liquid is small, the back-pressure due to compression of entrapped gases in the capillaries is negligible and the parabolic rate is essentially unaffected. As the entrapped gases are swept into the center of the specimen and compressed by the more slowly penetrating liquids, the back-pressure is built up to a significant magnitude and the total pressure at the liquid head is reduced resulting in

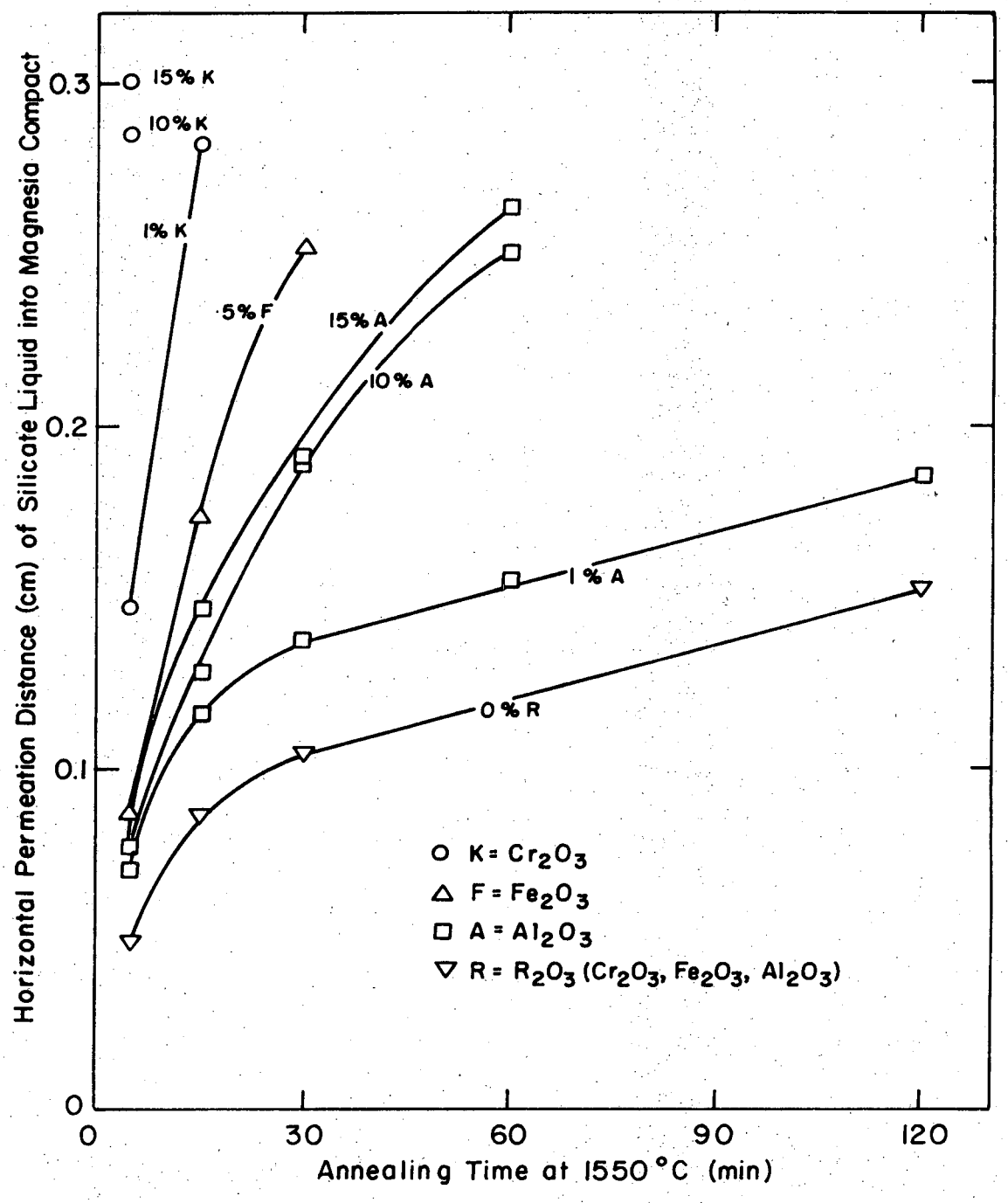

Figure 18.

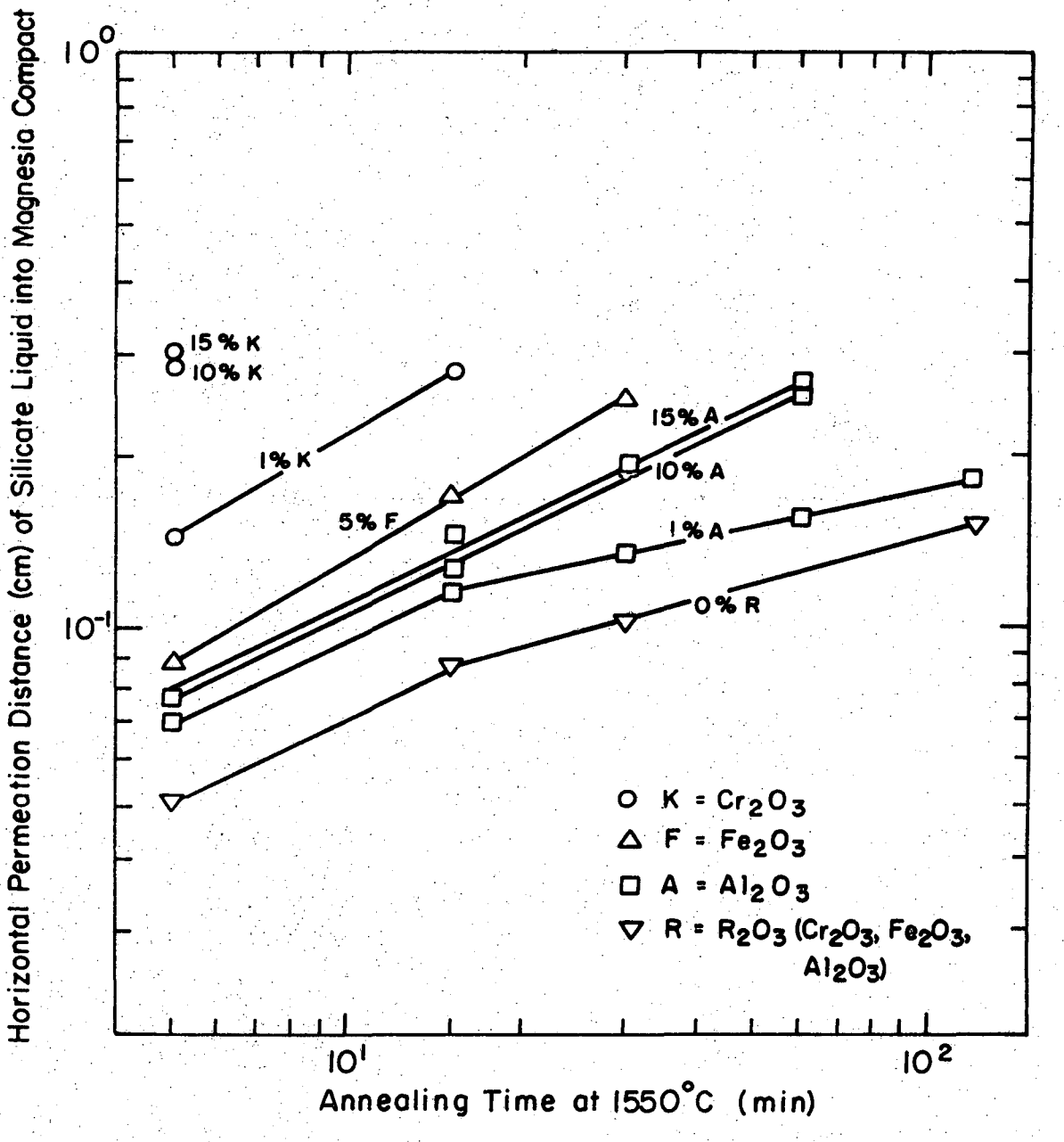
Horizontal Permeation Distance (cm) of Silicate Liquid into Magnesia Compact
10^0
10^-1
10^1
10^2
Annealing Time at 1550°C (min)
15% K
10% K
1% K
5% F
15% A
10% A
1% A
0% R
O K = Cr2O3
△ F = Fe2O3
□ A = Al2O3
▽ R = R2O3 (Cr2O3, Fe2O3, Al2O3)
XBL726-6366

Figure 19.

negative deviations from the initial one-half slope. When the back pressure becomes equal to the capillary pressure, a steady state or end point is reached.

The faster permeating liquids, such as those containing Cr_2O_3 and low Fe_2O_3 contents and thus with relatively larger driving forces for wetting (as will be seen later), bypass the smaller closed-end channels. The entrapped gases are then dispersed in small pockets instead of being segregated in the center of the specimen, as shown schematically in Fig. 20. These gases are compressed in each of the pockets as before. Penetration distance then is observed throughout the compacts according to an approximate parabolic rate.

The rate of capillary flow, given by Eq. (4) as developed in Section II, is controlled by the radius of the capillary, the viscosity of the liquid, and the total pressure acting at the head of the penetrating liquid. Although the radius of the capillaries is unknown, the average radius can be considered to be a constant since the MgO compacts were prepared at the same time in the same way. The viscosities of the different experimental silicate liquids are also unknown, but they can be considered not to vary too greatly because of the high O/Si ratios of the liquids. The observed differences could be produced by chemical reaction effect, and will be discussed below.

B. Chemical Reaction Effects

The capillary pressure of wetting is determined by the driving force for wetting which is indicated by the magnitude of the contact angle in a sessile drop experiment: the smaller the contact angle, the larger the driving force for wetting. Spreading occurs when the driving force for

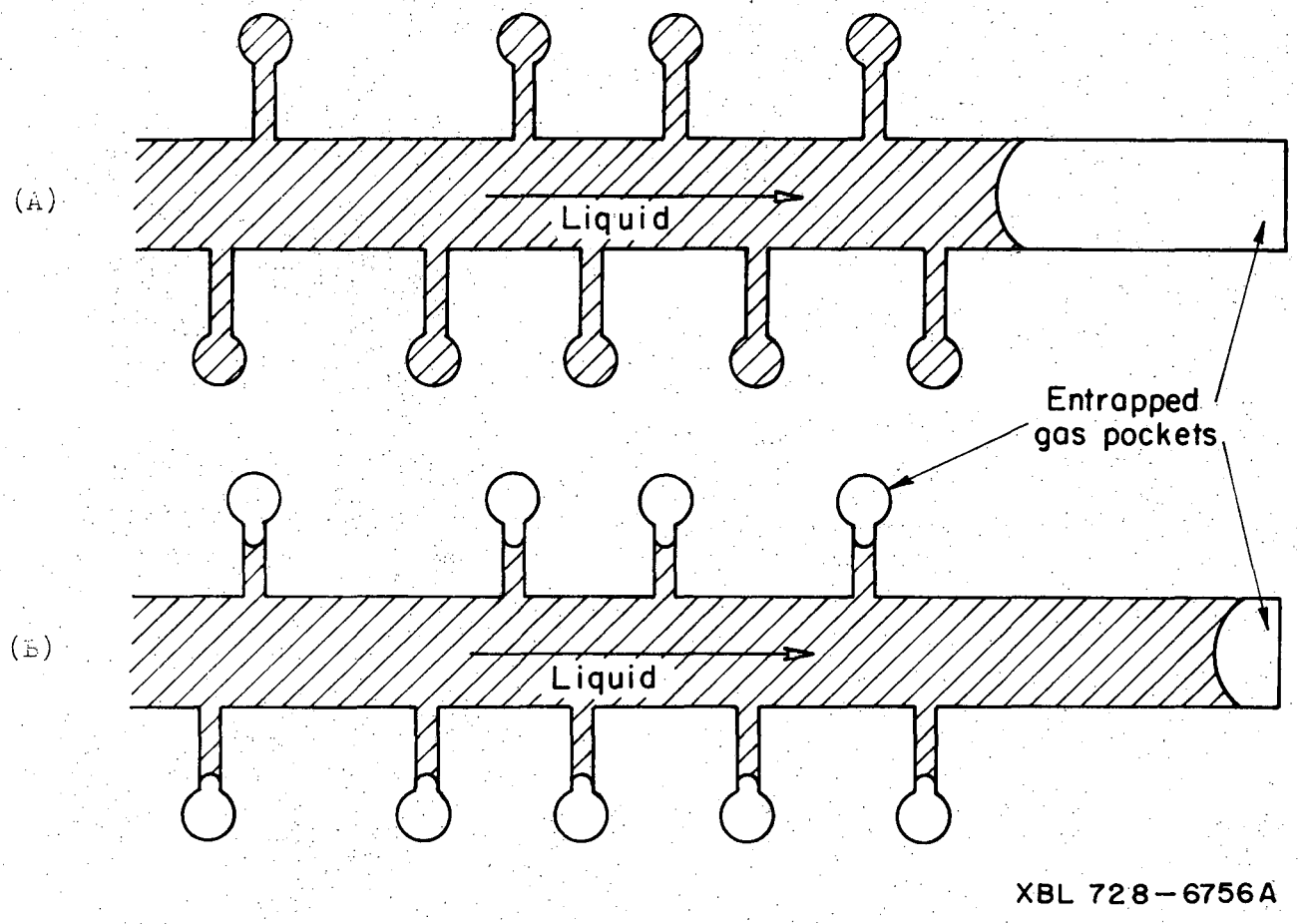

Figure 20A and 20B.

wetting exceeds the energy necessary to extend the liquid surface ($\gamma_{sv}-\gamma_{sl}>\gamma_{lv}$). Figure 21 shows the contact angles of different silicate liquids on a (100) face of MgO single crystals at 1550°C in air, as reported by Aksay.[10] The contact angle of CMS liquid on MgO is about 47°. With additions of sesquioxides (R_2O_3) to the liquid, the contact angle decreases. Spreading occurred when 3% or more Cr_2O_3 was added. Constant contact angles of 15° and 35° were obtained when 3% or more of Fe_2O_3 and 5% or more of Al_2O_3 were added, respectively.

When R_2O_3 is present in the liquid, a chemical reaction could occur at the solid-liquid interface if the phases are not in thermodynamic equilibrium. The nature of this interface reaction and its effect on the contact angle have been discussed by Aksay:[10]

$$R_2O_{3(\text{in liquid})} + MgO_{(\text{substrate})} \rightarrow MgR_2O_{4(\text{solid})}. \qquad (58)$$

If the MgO is unsaturated with respect to MgR_2O_4, the reaction product MgR_2O_4 will continue to be dissolved until the chemical potential or activities of R_2O_3 in the liquid and substrate are the same. If the MgO becomes saturated before the excess R_2O_3 in the liquid becomes exhausted, then a separate MgR_2O_4 phase will form at the interface. At constant temperature and pressure:

$$\mu(R_2O_3 \text{ in MgO}) = \mu_o(R_2O_3) + RT\ln a(R_2O_3 \text{ in MgO}). \qquad (59)$$

$$\mu(R_2O_{3\text{ in liquid}}) = \mu_o(R_2O_3) + RT\ln a(R_2O_{3\text{ in liquid}}). \qquad (60)$$

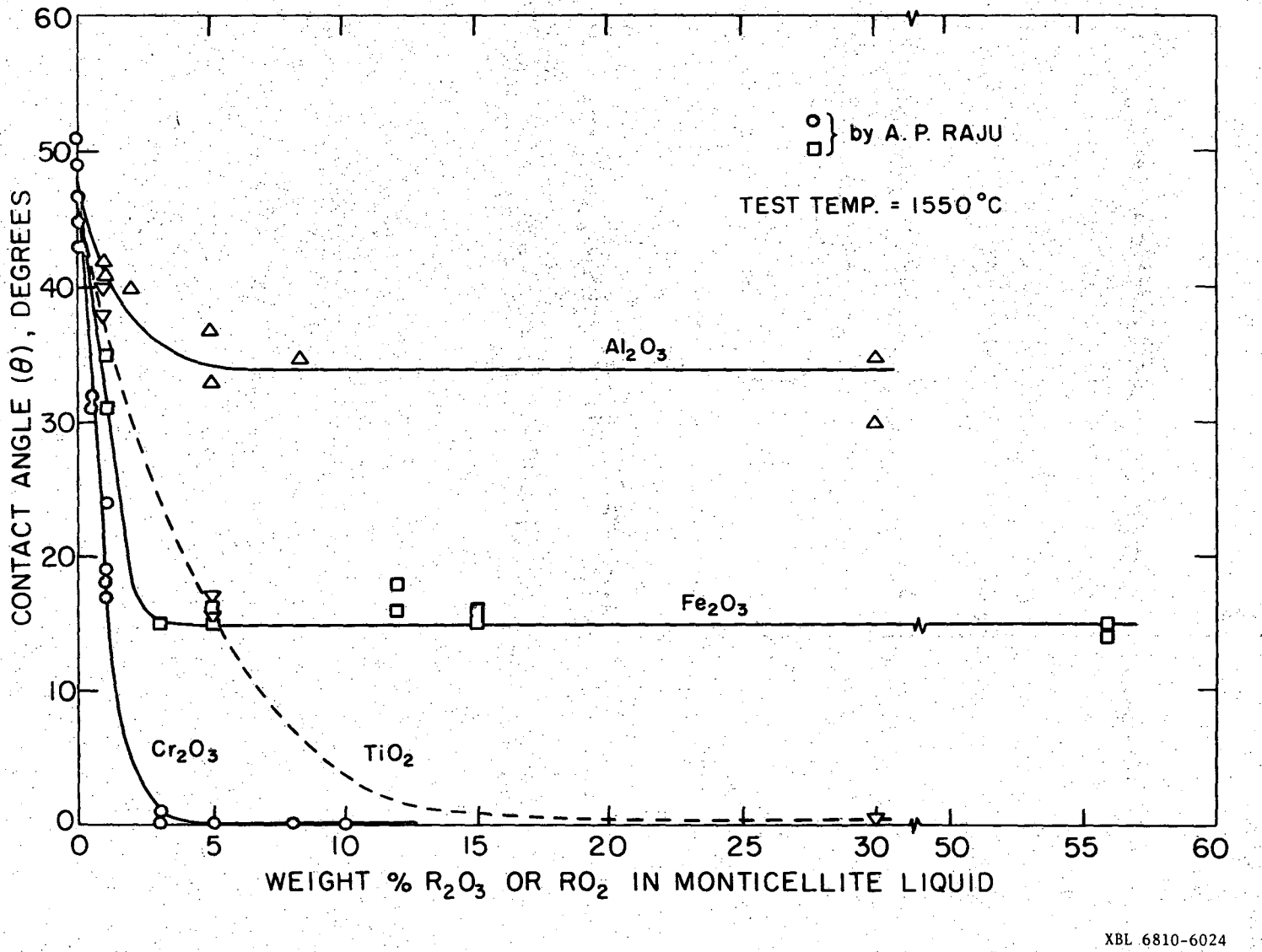
60
50
40
30
20
10
0
CONTACT ANGLE (θ), DEGREES
by A. P. RAJU
TEST TEMP. = 1550°C
Al2O3
Fe2O3
Cr2O3
TiO2
0
5
10
15
20
25
30
50
55
60
WEIGHT % R2O3 OR RO2 IN MONTICELLITE LIQUID
XBL 6810-6024

Figure 21.

Subtraction of (60) from (59) results in

$$\mu(R_2O_3 \text{ in MgO}) - \mu(R_2O_3 \text{ in liquid}) = (\Delta\mu)^{sl}$$

$$= RT \ln \frac{a(R_2O_3 \text{ in MgO})}{a(R_2O_3 \text{ in liquid})} \quad . \tag{61}$$

$(\Delta\mu)^{sl}$, which is equivalent to $\sum_j \mu_j^{sl}\Gamma_j^{sl}$ as shown in Section II, is always a negative quantity of free energy change for spontaneous reaction. Therefore, as long as $(\Delta\mu)^{sl}$ exists, the solid-liquid (sl) interfacial free energy will be reduced, and the net driving force for wetting will increase by its contribution.

If it is assumed that the interface reaction in these systems is always fast, the magnitude of the $(\Delta\mu)^{sl}$ contribution to wetting will then depend upon the diffusion kinetics in the system. Diffusion of R^{+3} ions in the MgO compact is postulated to be the controlling step of the rate of reaction due to nonequilibrium in the bulk system. The diffusion flux in MgO, given by $J_i = - D_i \frac{dC_i}{dx} = - C\, D_i \frac{dN_i}{dx}$ (where C_i = concentration of species 'i', C = total concentration which is a constant, N_i = mole fraction of species 'i' in MgO), determines the rate of reaching bulk chemical equilibrium. If the flux is large, i.e. either D_i or $\frac{dC_i}{dx}$ or both are large, the rate of reaching bulk chemical equilibrium is fast; thus, the time for the system, or for the effective area just ahead of the liquid to be wetted, to reach equilibrium is relatively short. Then $a(R_2O_3 \text{ in MgO}) \tilde{\sim} a(R_2O_3 \text{ in liquid})$, and the $(\Delta\mu)^{sl}$ contribution to

wetting due to a sl interface reaction is small.

The diffusivity of Fe^{+2} and Fe^{+3} in MgO at 1600°C is in the range of 3.1×10^{-9} cm^2/sec;[12] Cr^{+3} 1.3×10^{-11} cm^2/sec;[14] and Al^{+3} 1.6×10^{-9} cm^2/sec calculated from published data.[15] Accordingly, at 1600°C $D_{Fe} > D_{Al^{+3}} >> D_{Cr^{+3}}$. Slow diffusion of Cr^{+3} in MgO results in the MgO area just ahead of the wetting liquid to be unsaturated and reactive with Cr_2O_3 in the liquid. Since the reactivity depends on the ratio of

$$\frac{a(R_2O_3 \text{ in MgO})}{a(R_2O_3 \text{ in liquid})}$$

there is a significant $(\Delta\mu)^{sl}$ contribution to the driving force for wetting, and the contact angle decreases with increase of the content of Cr_2O_3 in the liquid. The contribution apparently was large enough to result in spreading with 3% or more Cr_2O_3 in the liquid. The diffusion of Fe in MgO appears to be comparable to the sl interfacial reaction rate thus diminishing the contribution of $(\Delta\mu)^{sl}$ to wetting. When sufficient amounts of Fe_2O_3 are added to the liquid, the diffusion flux to the area ahead of the wetting liquid results in essential equilibrium of the solid with the liquid at the three-phase junction; the $(\Delta\mu)^{sl}$ contribution to wetting is then practically absent, and a steady state constant contact angle results. Intermediate rates of diffusion and a low solubility limit (less than 1 wt% at 1550°C) of Al_2O_3 in MgO results in bulk phase equilibrium in the region of the advancing liquid. The $(\Delta\mu)^{sl}$ contribution to wetting then is not significant and a constant contact angle

is attained.

The indicated correlation of the rate of permeation and the wetting behavior of the liquid on the solid is supported by a comparison of the results of Figs. 18 and 19 with Fig. 21, except for the lack of significant permeations by the liquids containing 45% and 55% Fe_2O_3 even though these liquids wet the MgO solid. This condition is due to fast diffusion of Fe ions in MgO and the high solubility limit of iron oxide in MgO resulting in a fast and large bulk reaction. Product layers of spinel then build up rapidly at the solid-liquid interfaces. As a result, all the open channels are closed off during the initial stages of permeation. Further discussions on the corresponding microstructure development will be covered in the next section.

C. Microstructure Effects

MgO compacts with 2 hours of additional annealing in air at 1550°C did not have any significant changes in their density (ρ_{th} = 92.5%) or microstructures. Compacts without and with annealing are shown in Figs. 16 and 22, respectively. Figures 16a and 22a are selected sections showing both the less dense and denser areas in the specimens. In the less dense areas, the grains are smaller than the grains in the denser areas. Figures 16b and 22b show the same specimens at a higher magnification. Discontinuous grain growths, similar distribution of pores both inside the grains and at the grain boundaries, and similar grain sizes are observed.

With liquid permeation, however, significant microstructure changes occurred. Figures 23a and 23b (low and high magnification) show the microstructure of an MgO compact permeated by a liquid containing 15%

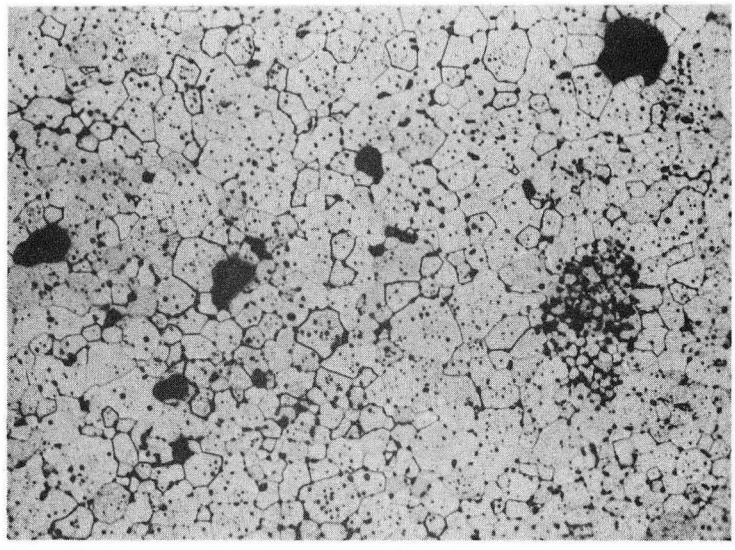

Figure 22a.

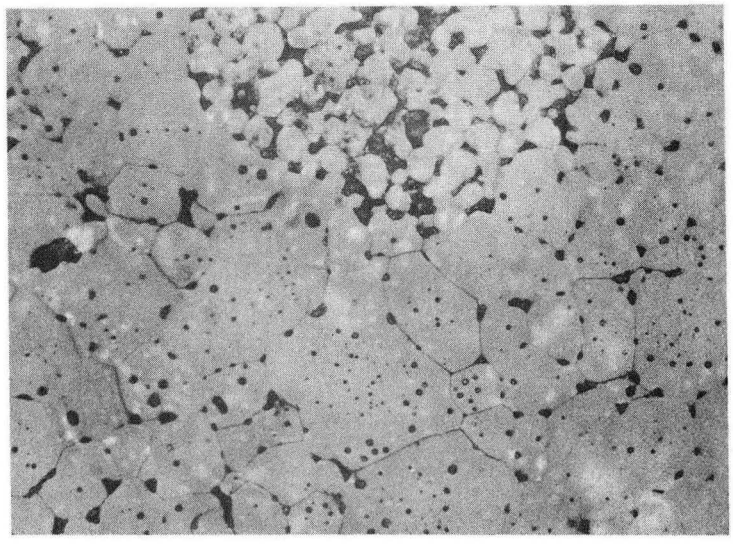

XBB-726-3054

Figure 22b.

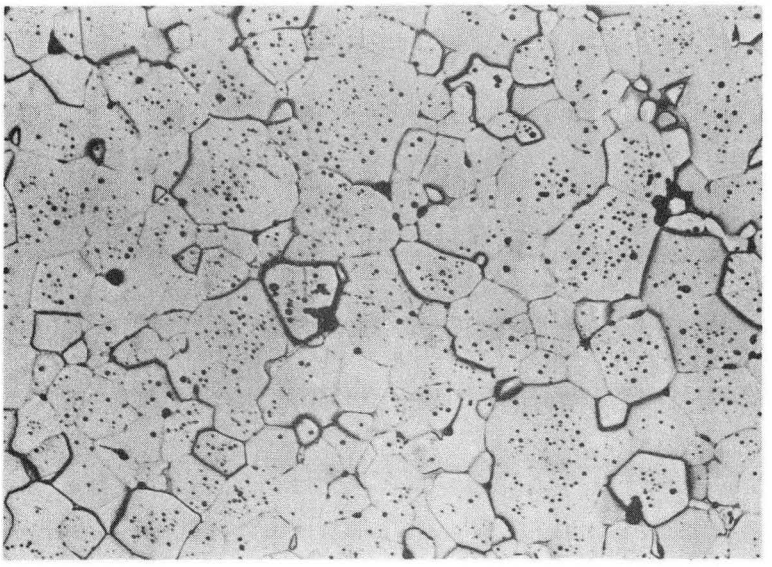

Figure 23a.

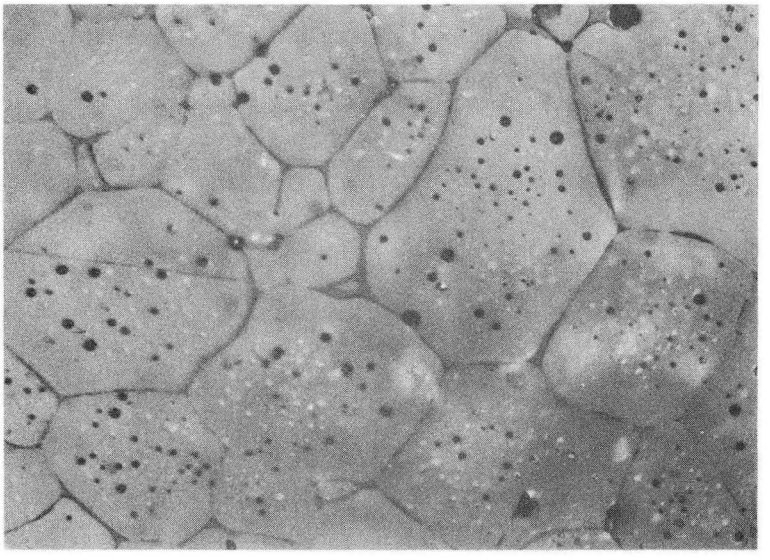

XBB-726-3481

Figure 23b.

Cr_2O_3 after 5 minutes at 1550°C. A comparison with Figs. 16 and 22 shows the appearance of thin films of liquid along most of the grain boundaries with an elimination of the pores along these boundaries, and grain growth. Figures 24, 25, 26 and 27 show the microstructures of the compacts permeated by liquids containing low amounts of Cr_2O_3, low amounts of Fe_2O_3, and low and high amounts of Al_2O_3, respectively, after 2 hours at 1550°C. A comparison with Fig. 23 shows the presence of lesser amounts of liquid films at the grain boundaries and varying amounts of liquid films at the grain boundaries and varying amounts of grain growth. Figures 28a and 28b (low and high magnification) show the microstructure permeated by CMS liquid after 2 hours at 1550°C. In the denser areas, liquid can be observed primarily at the triple points, and little grain growth has occurred. On the other hand, in the less dense areas, most of the grains are enveloped by the liquid and have grown larger and more spherical.

The observed microstructural changes must be due to material redistribution as a result of some solution and reprecipitation process either under conditions of bulk thermodynamic equilibrium or non-equilibrium. A solution-precipitation process arises when two adjoining regions in the compact have different chemical potentials due either to differences in composition or structure defects. Solubility limits of the solid in the liquid in such two regions are different. As a result, a concentration gradient between the two regions is established in the liquid, and material migrates from the high chemical potential region to the lower chemical potential region where precipitation occurs because of supersaturation.

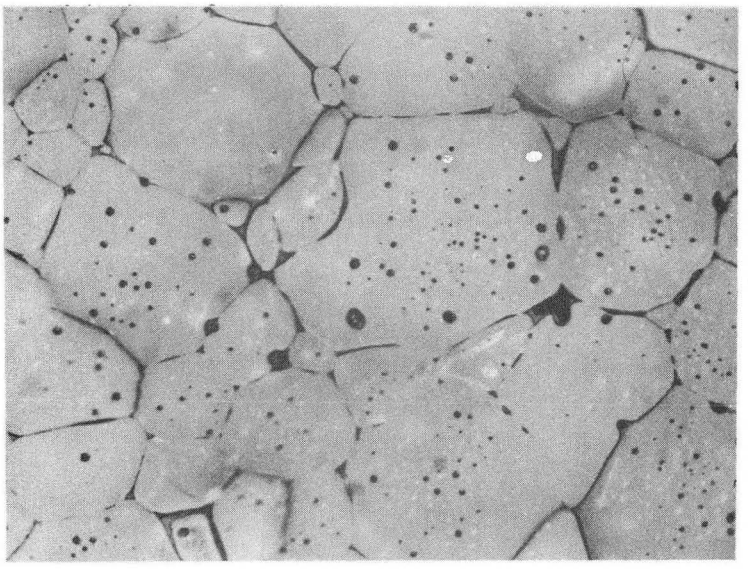

Figure 24.

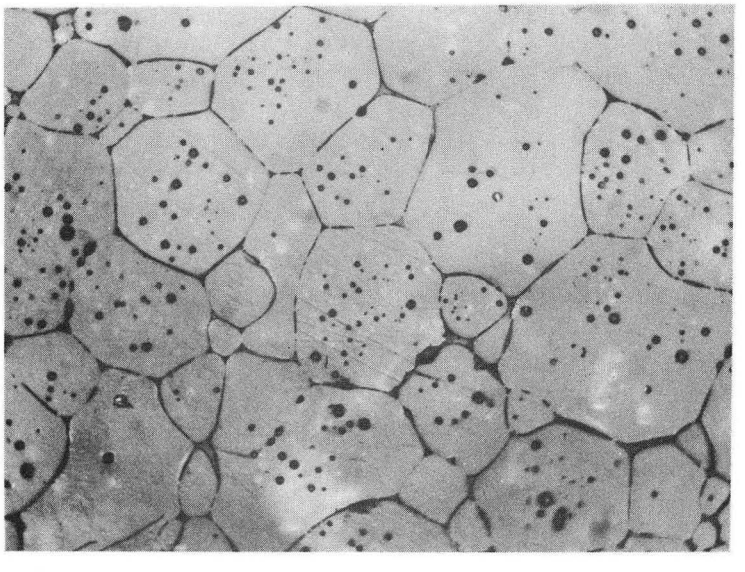

XBB-726-3052

Figure 25.

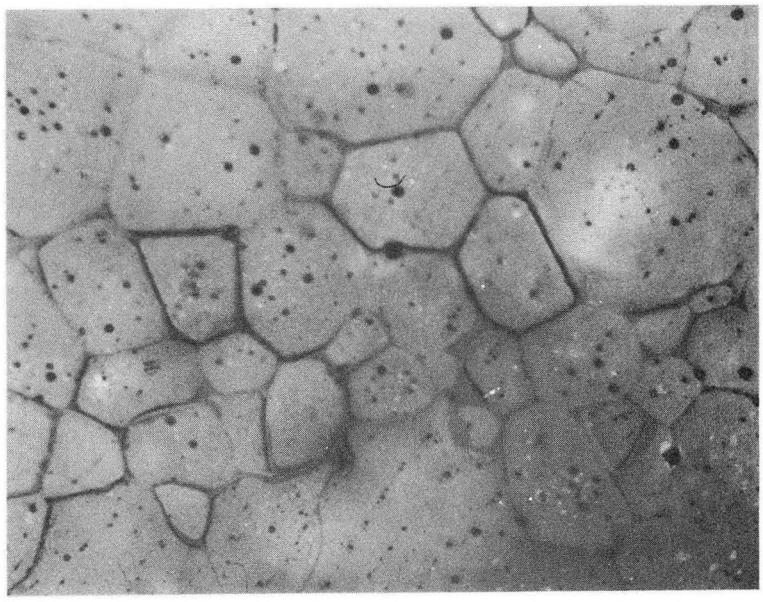

Figure 26.

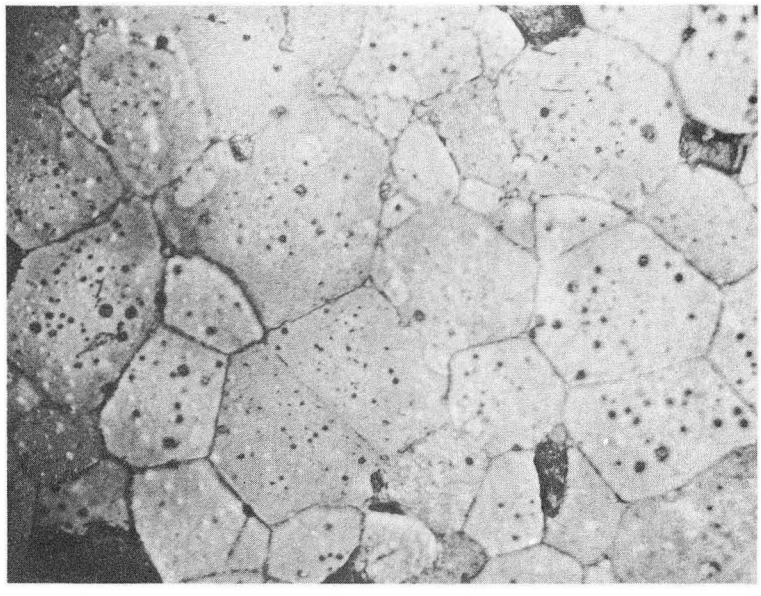

XBB-726-3482

Figure 27.

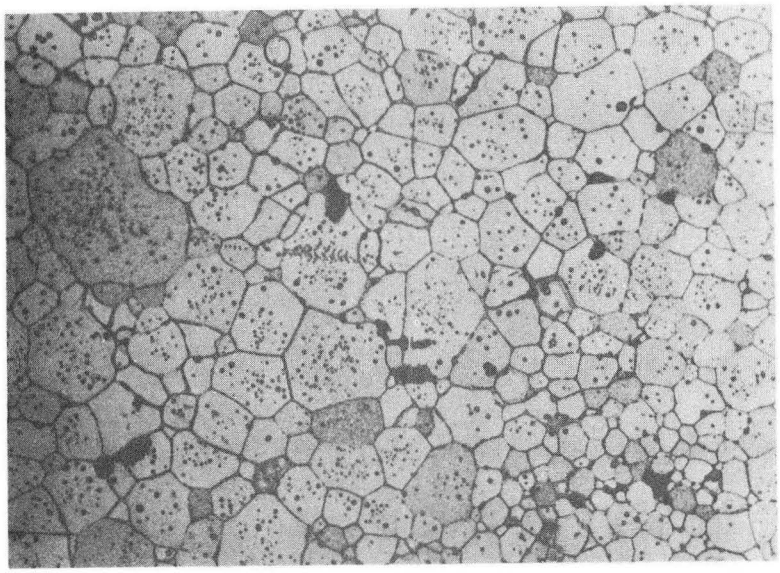

Figure 28a.

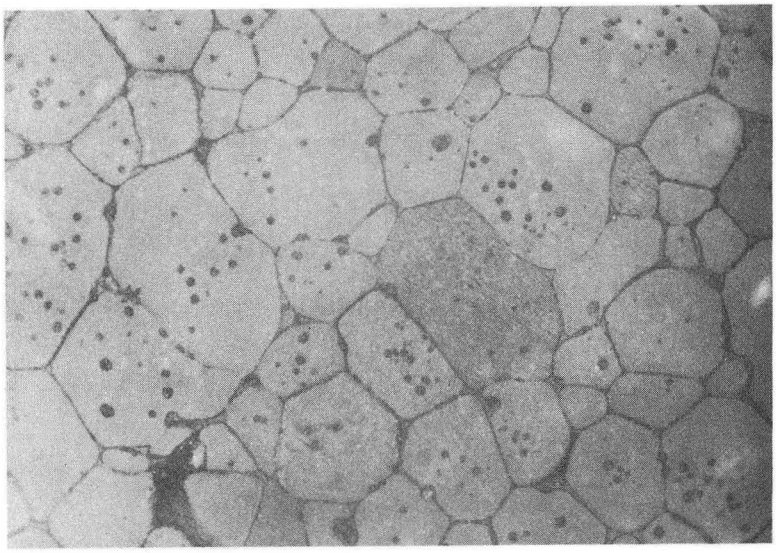

XBB-726-3483

Figure 28b.

The Thomson-Freundlich equation was thermodynamically derived[16] which shows that different solubility limits of solid in liquid exist for particles of different sizes even when their chemical compositions are the same and when bulk thermodynamic equilibrium exists between the solid and liquid. The equation states:

$$\ln \left\{ \frac{\left[X^{l}_{s(sat)}\right]_{r}}{\left[X^{l}_{s(sat)}\right]_{\infty}} \right\} = \frac{2M\gamma_{sl}}{rRT\rho} . \qquad (62)$$

$[X^{l}_{s(sat)}]_{r}$ and $[X^{l}_{s(sat)}]_{\infty}$ are solubility limits of the solid in the liquid when its radius of curvature is equal to r and infinity (flat surface), respectively. The other terms are:

γ_{sl} = interfacial free energy between the solid and the liquid

M = molecular weight of the solid

T = absolute temperature

ρ = density of the solid

R = gas constant

Accordingly, solids are dissolved at the regions with small radius of curvature (convex surfaces, small grains, etc.) and re-precipitated at the regions with large radius of curvature (concave or flat surfaces, large grains, etc.). An extension of the Thomson-Freundlich equation to other sources of excess free energy suggest that solution would also occur in the regions with higher amounts of atomic defects (high chemical potential regions) and precipitation in the regions with "perfect" structures (low chemical potential regions) irrespective of curvature,

assuming that such regions existed at the time the liquid reached them.

Material redistribution is also dependent on the lack of bulk thermodynamic equilibrium between the solid and liquid phases. CMS liquids with sesquioxide additions are not in equilibrium with MgO and thus will dissolve MgO at 1550°C according to the respective phase diagrams[10] shown in Figs. 29, 30, and 31 to reach their saturation limits. MgO will also dissolve sesquioxides from the liquids to reach saturation limits or equivalent chemical potentials in the solid and liquid (Fig. 32). Use of "reactive liquids, such as those with higher amounts of Cr_2O_3 and associated large $(\Delta\mu)^{sl}$, thus result in a significant reduction of the s-l interfacial free energy and solution of some of the MgO. This condition generally decreases the dihedral angle to zero and allows the liquid to penetrate the grain boundary. The liquid then has a chance to distribute itself along the grain boundaries with elimination of previously existing pores and occurrence of grain growth. Less "reactive" liquids, such as those with low Cr_2O_3 and low Fe_2O_3 contents, and those with Al_2O_3, will have lesser reductions of the s-l interfacial free energy and solution of smaller amounts of magnesia. The microstructures reflect the effect of these mechanisms.

With "non-reactive" liquids, such as CMS liquid in contact with MgO at 1550°C, the dihedral angle is relatively large under equilibrium conditions. Permeating into the denser areas in the compacts, these liquids can normally only penetrate along the triple lines. A limited amount of penetration, however, can occur along boundaries with highly misoriented grains and large amounts of structural defects by a solution and precipitation process. Therefore, most of the pores at the grain boundaries

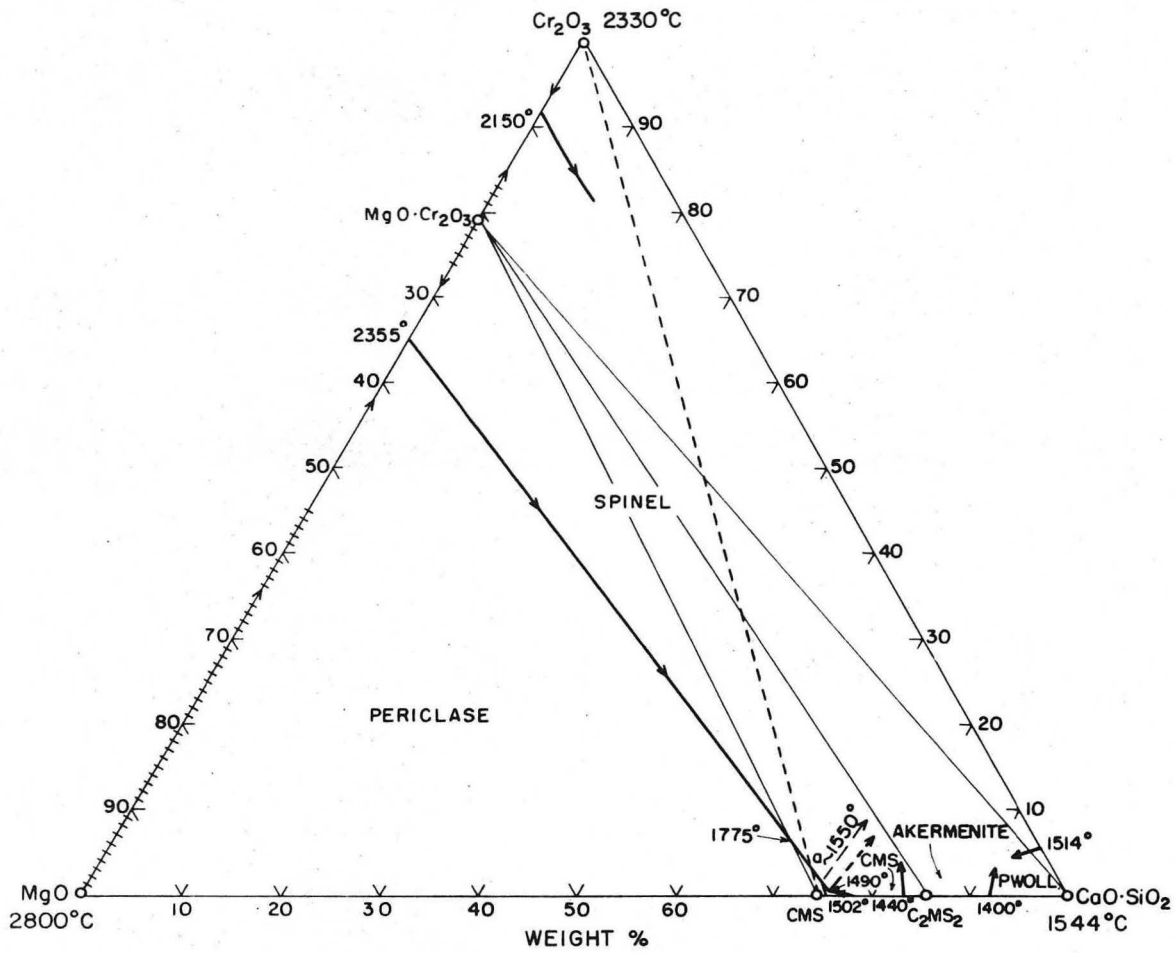
Cr_2O_3 2330°C
2150°
$MgO \cdot Cr_2O_3$
2355°
SPINEL
PERICLASE
1775°
1550°
AKERMENITE
1514°
CMS
1490°
PWOLL
MgO
2800°C
CMS
1502°
1440°
C_2MS_2
1400°
$CaO \cdot SiO_2$
1544°C
WEIGHT %
XBL 6810-6029

Figure 29.

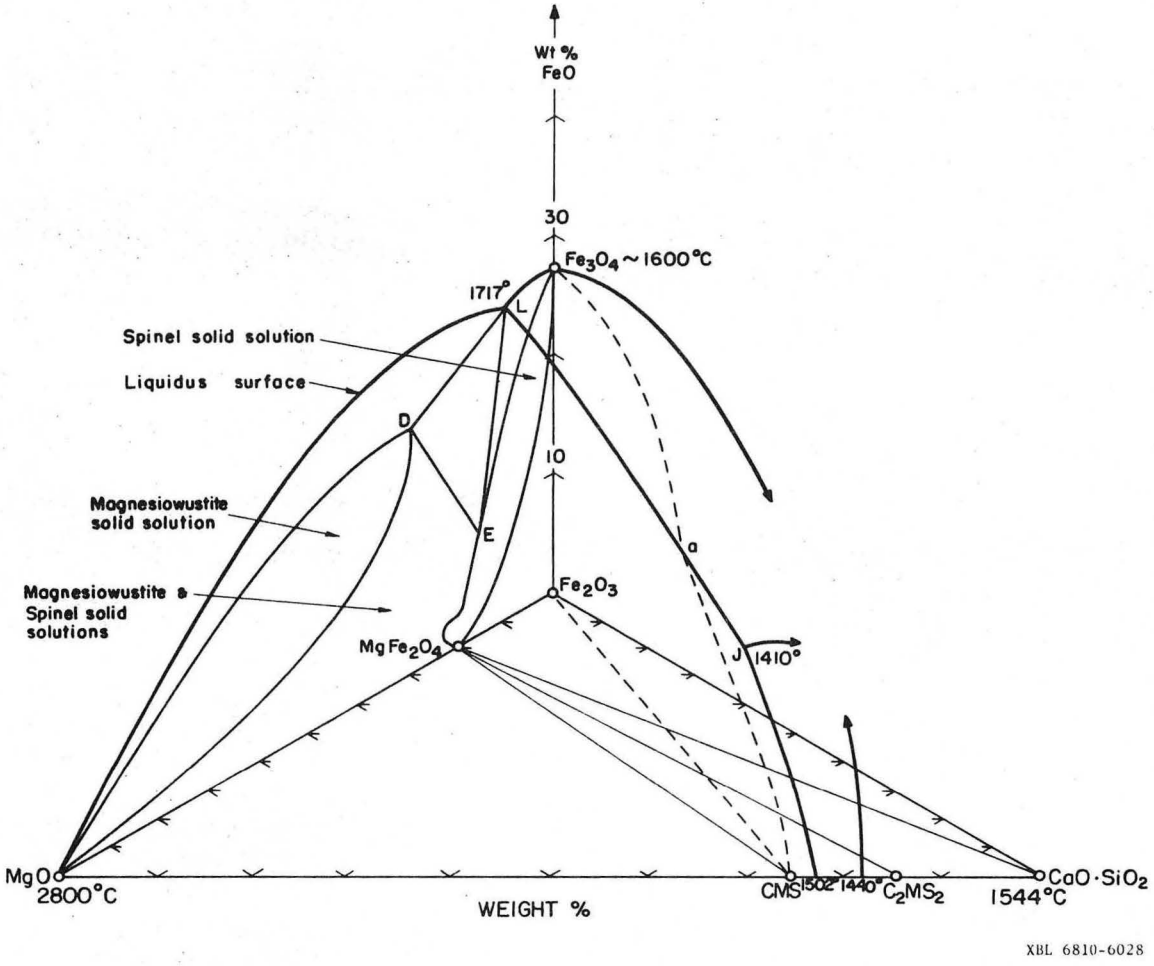

Figure 30.

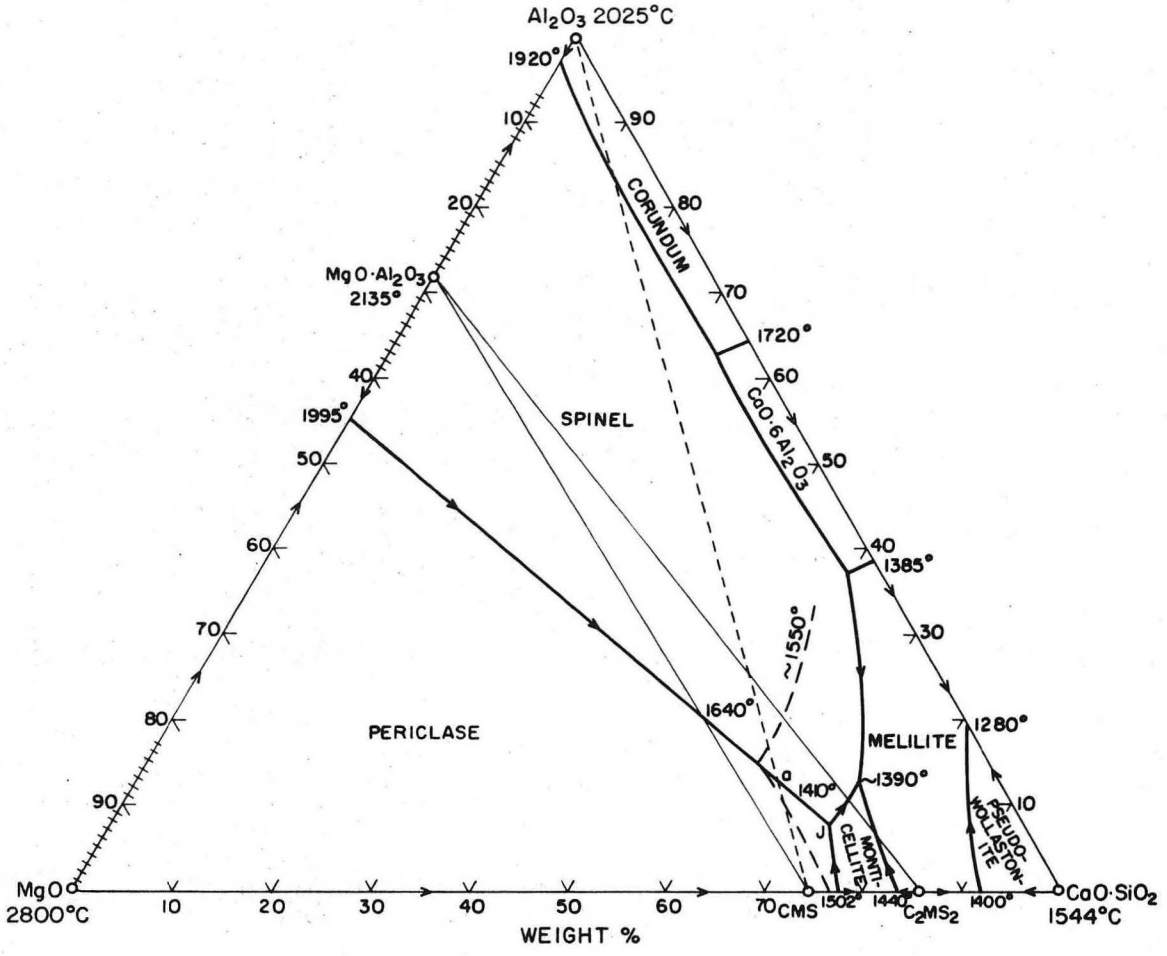

XBL 6810-6031

Figure 31.

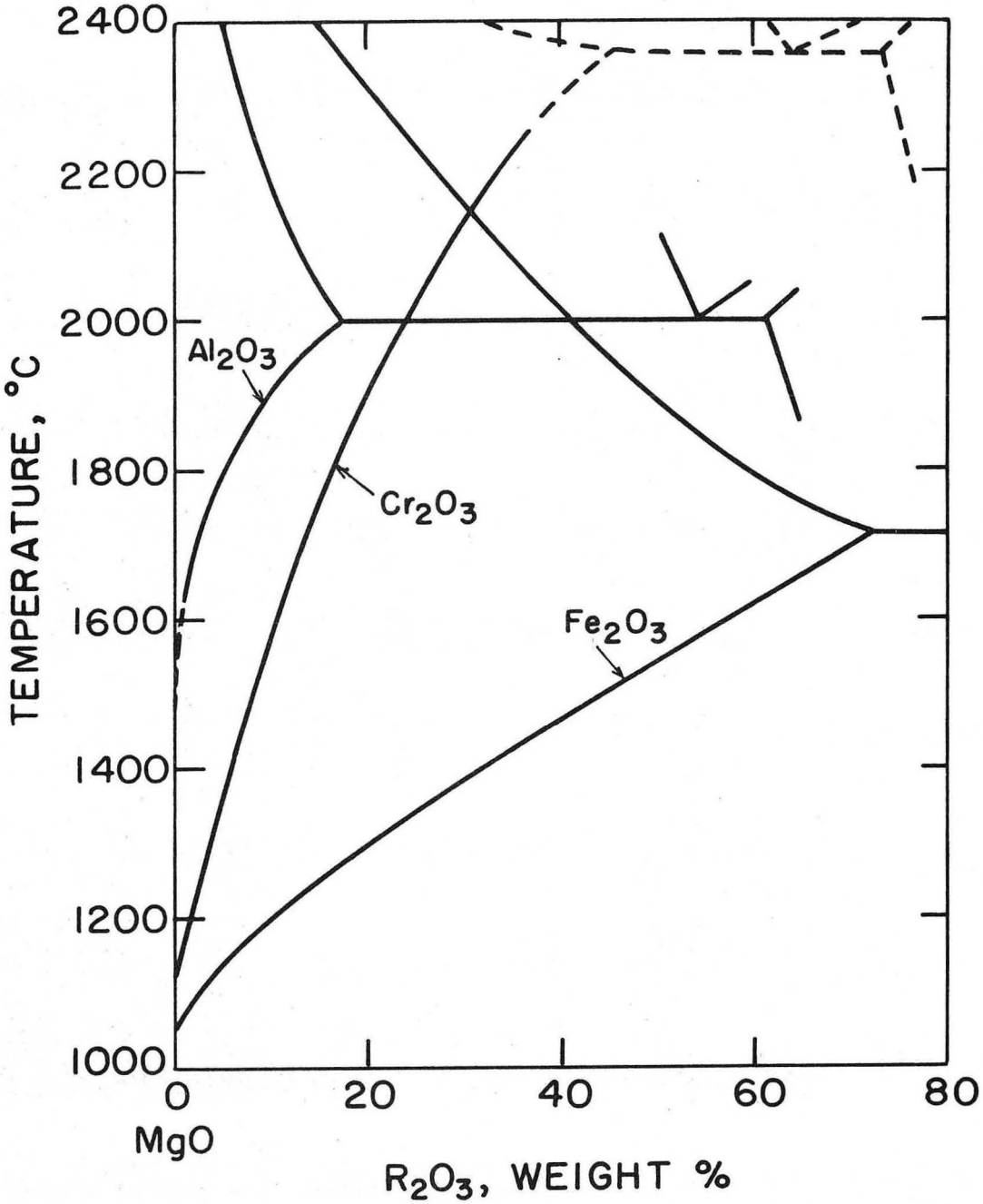

XBL 6810-6026

Figure 32.

still remain and grain growth is limited and localized. In the less dense areas, large and numerous channels are available that could be permeated by liquid resulting in the presence of relatively large amounts of liquid surrounding most of the grains. The small grains in these areas exhibit a relatively larger growth in comparison with the large grains in the denser areas, as shown in Figs. 28a and 28b. These observations are verified by the Thomson-Freundlich relationship.

The liquids discussed so far did not have sufficient amounts of sesquioxides added to saturate them; the driving force for the reactions was then to attain uniform chemical potentials in the systems which were insufficient to form a separate spinel phase. However, the high iron oxide-containing liquids (45% or 55% Fe_2O_3 additions to CMS), at 1550°C were saturated with spinel and had an excess of spinel. These liquids when in contact with MgO, reacted to saturate the MgO with spinel and to form spinel layers at the interfaces because of the fast chemical interdiffusivities of Fe ions in MgO. This growth of the grains due to saturation led to the closing off of the available open channels. The reaction layers were not subsequently dissolved because of the excess iron oxide in the liquid. The reaction zone can be seen in Figs. 33a and 33b which show the s-l interface of the 45% Fe_2O_3 liquid permeation specimens after 5 minutes and 2 hours annealing at 1550°C, respectively. The light colored dendrites are spinel which precipitated during cooling of the specimens. The microcracks apparently are produced by differential stresses that developed during cooling. Figures 34 and 35 show the interior areas of these two specimens. No liquid phase appears in either one of them, and the microstructures are similar to those of the MgO

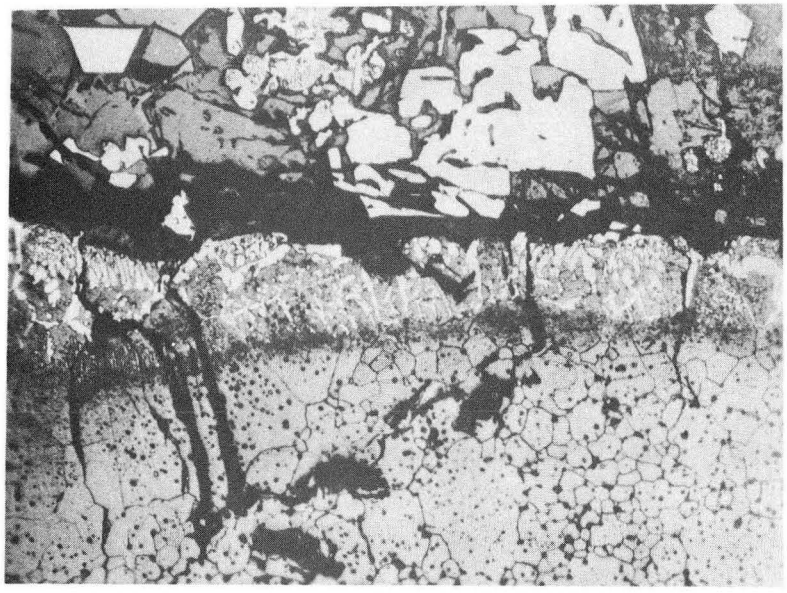

Figure 33a.

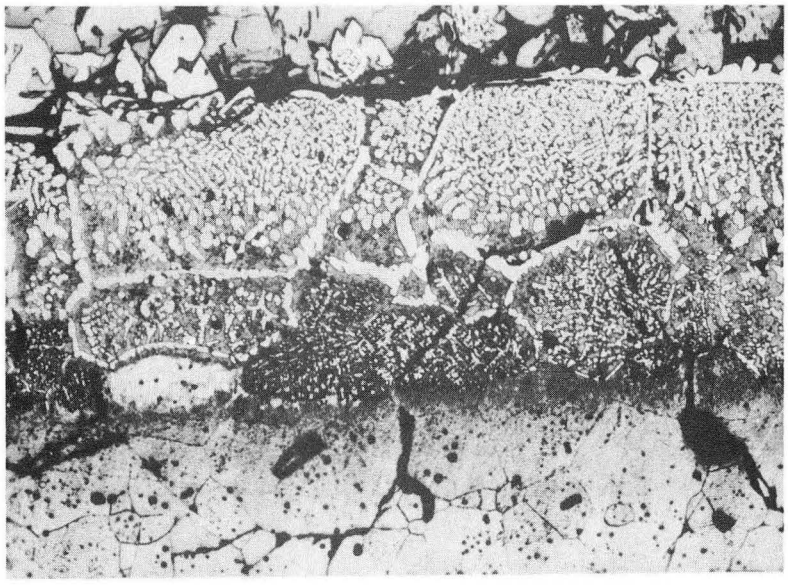

XBB-726-3060

Figure 33b.

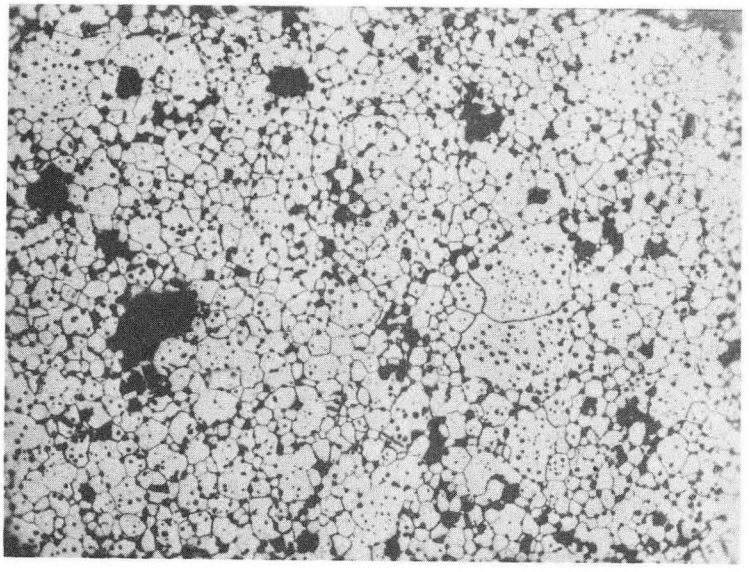

Figure 34a.

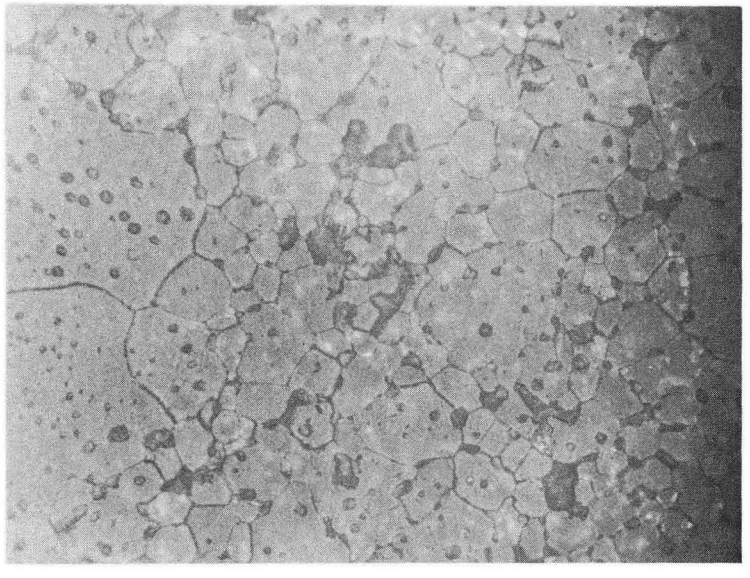

XBB-726-3059

Figure 34b.

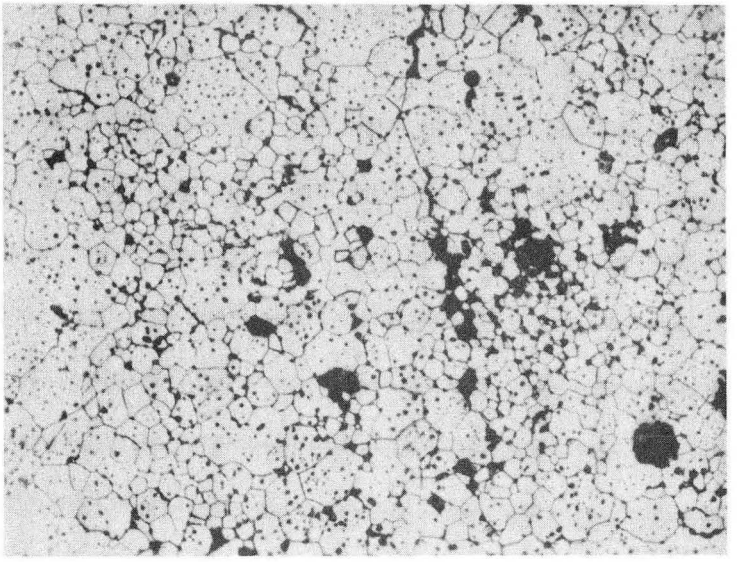

Figure 35a.

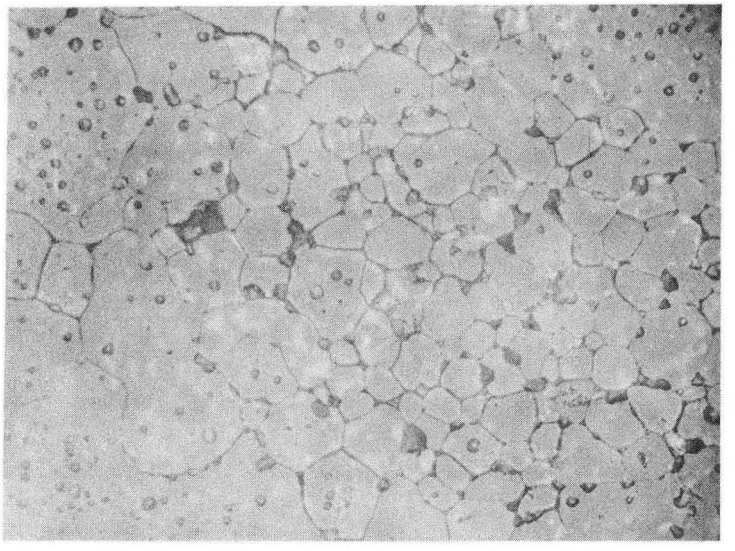

XBB-726-3061

Figure 35b.

compacts shown in Figs. 16 and 22. This observation further indicates that the discussed microstructural changes in the compacts occurred only in the presence of liquids that permeated the MgO specimens.

VI. CONCLUSIONS

A. Permeation Studies

Permeation rate of a viscous liquid into a "homogeneous" compact with fine capillaries depends mainly on the driving force for wetting, which in turn depends greatly on the chemical changes that may occur at the interfaces. Differences in hydraulic head effects for upward versus downward permeation were found to be insignificant for small samples.

(1) If no chemical reactions occur at the interfaces, the permeation rate depends only on the driving force for wetting due to a lower γ_{sl} than γ_{sv} and is usually the slowest in comparison with conditions where a reaction may occur.

(2) If a s-l interface reaction is significant at the three-phase junction of an advancing liquid as a result of slow diffusion of the product species into the bulk ahead of the advancing liquid and slow depletion of reactants, the contribution of the free energy of the reaction to wetting is significant and the permeation rate usually is fast.

(3) In cases where either fast diffusion of the product species into the solid or depletion of reactants occurs, the s-l interface reaction contribution to wetting is less significant and the permeation rate is reduced.

Fast bulk reactions of the liquid and the solid and the presence of excess sesquioxide in the liquid usually result in the rapid buildup of a product layer at the s-l interface. These product layers can block the open capillary channels of the solid and prevent liquid permeation into the interior.

The average permeation distance of a viscous liquid into a compact with fine capillaries increases parabolically with time during the initial stages. A negative deviation from this relationship usually results at later stages when the back-pressure developed by compression of entrapped gases becomes significant. If the driving force for wetting is large and the permeation rate is fast, the liquid may bypass gases entrapped in smaller channels by moving along in the larger channels resulting in a dispersion of pockets of gas instead of a segregation in the center of the specimen; parabolic rates are thus maintained for greater penetration distances.

B. Microstructure Effects

The microstructure of a relatively dense solid compact is significantly affected by a permeating liquid. The degree of material redistribution in the solid by a solution-precipitation process is dependent on the degree of reactivity of the liquid with the solid.

(1) If a significant s-l interface reaction is present contributing to the reduction of the s-l interfacial energy, the dihedral angle is usually zero and the liquid penetrates along the grain boundaries. Material is removed from high chemical potential regions to low chemical potential regions. As a result, pores at the grain boundaries are eliminated, liquid films occur along the boundaries, and growth of the grains is observed.

(2) If the s-l interface reaction is less significant or absent, the dihedral angle in the more dense regions is larger and the liquid penetrates primarily along triple lines. Pores along grain boundaries that are not penetrated by the liquid thus are not eliminated. In less

dense regions, containing more pores and probably more structural defects, however, the liquid penetrates the grain boundaries by a solution-precipitation process.

Fast diffusion of product species at the s-l interfaces into the bulk, and presence of excess R_2O_3 in the liquid results in the formation of product layers at these interfaces and the closing of open channels. No significant liquid permeation into the compact then occurs. Internal stresses develop on cooling due to mismatches of thermal expansion and are frequently large enough to create microcracks.

APPENDIX I

The Motion of a Viscous Fluid in a Straight Circular Tube

Assuming the fluid flow is laminar, a configuration as shown in Fig. 36 can be used for illustration. A circular tube with radius a contains an incompressible and viscous fluid inside. There is a force exerted on an arbitrary cross section of a cylindrical mass of the fluid of radius r due to the pressure difference, $P_1 - P_2$ between two arbitrary points with distance l apart from each other in the fluid. On the other hand, there is also an opposing force due to the friction on the curved surface.

The exerting force = $(P_1-P_2)\pi r^2$

The opposing force = $2\pi rl\tau$

Where τ is the shearing stress produced by the layer slipping over each other. Equating the two forces, we obtain

$$-\tau = \frac{(P_1-P_2)}{l}\left(\frac{r}{2}\right) \tag{63}$$

$$\because \tau = \eta \frac{du}{dr} \tag{64}$$

Where η is viscosity of the fluid and u is any velocity of the intermediate layers slipping past each other. Substituting Eq. (64) into Eq. (63), we have

$$du = \frac{-(P_1-P_2)}{\eta l}\frac{r}{2}\,dr. \tag{65}$$

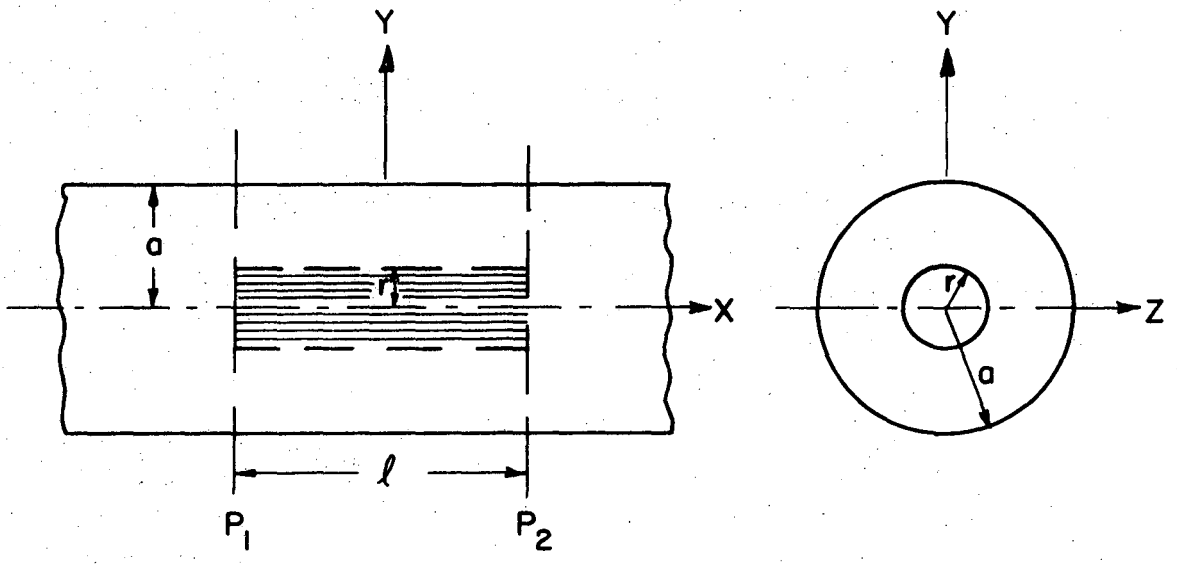

XBL 726-6370

Figure 36.

Integrating Eq. (65) and determining the constant of integration so that the velocity is zero at the wall (r = a), we have

$$u = \frac{(P_2-P_1)}{4\eta l}(r^2-a^2). \tag{66}$$

The discharge rate of the fluid or quantity of fluid passing per unit time can now be evaluated as

$$Q = \int_o^a 2\pi r dr(u) = \frac{\pi a^4}{8\eta}\ \frac{(P_2-P_1)}{l}. \tag{67}$$

This equation, stating that the discharge rate is proportional to the pressure fall per unit length and to the fourth power of the radius of the tube, was first discovered by Poiseuille and is called the Poiseuille Law.

APPENDIX II

1. The Chemical Analysis of MgO Powder

Baker and Adamson Reagent No. 1917

Substance	Wt.%
Assay (MgO) (after ignition)	99.0
Insoluble in dilute HCl	0.020
Soluble in water	0.40
Loss on ignition	2.0
Ammonium hydroxide precipitate	0.020
Chloride (Cl)	0.010
Nitrite (NO_3)	0.005
Sulfate and sulfite (as SO_4)	0.005
Barium (Ba)	0.005
Calcium (Ca)	0.05
Heavy metals (as Pb)	0.003
Iron (Fe)	0.010
Manganese (Mn)	0.0005
Potassium (K)	0.005
Sodium (Na)	0.50
Stronium (Sr)	0.005
Silica (SiO_2)	0.040

2. The Chemical Analysis of $CaCO_3$ Powder

Baker and Adamson Reagent No. 1506

Substance	Wt.%
Assay ($CaCO_3$)	99.0
Insoluble in dilute HCl	0.010
NH_4OH precipitate	0.010
Chloride (Cl)	0.001
Oxidizing substance (as NO_3)	0.005
Sulfate (SO_4)	0.010
Ammonium (NH_4)	0.003
Barium (Ba)	0.005
Stronium (Sr)	0.10
Magnesium (Mg)	0.02
Potassium (K)	0.01
Sodium (Na)	0.10
Heavy metals (as Pb)	0.001
Iron (Fe)	0.002

3. SiO Powder

Ottawa Silica Flour

Substance	Wt.%
Silica (SiO_2)	99.8
Alumina (Al_2O_3)	0.1
Iron oxide (Fe_2O_3)	0.02
Calcium oxide and magnesium oxide (Ca), MgO)	0.1

4. The Chemical Analysis of Al_2O_3 Powder

Baker Analyzed Reagent No. 0536

Substance	Wt.%
Assay (Al_2O_3)	99.5
Loss on ignition	0.3
Chloride (Cl)	0.005
Sulfate (SO_4)	0.003
Heavy metals (as Pb)	0.0005
Iron (Fe)	0.001

5. Cr_2O_3 Powder

Baker Analyzed Reagent No. 1616. A chemical analysis was not performed.

6. The Chemical Analysis of Fe_2O_3 Powder

Baker Analyzed Reagent No. 2024

Substance	Wt.%
Assay (Fe_2O_3)	99.5
Insoluble in HCl	0.04
Phosphate (PO_4)	0.02
Sulfate (SO_4)	0.04
Copper (Cu)	0.003
Manganese (Mn)	0.03
Substances not precipitated by NH_4OH (as SO_4)	0.003
Zinc (Zn)	0.003

ACKNOWLEDGMENTS

I wish to express my special gratitude and sincere thanks to my teacher and research adviser, Professor Joseph A. Pask, for his patient guidance, helpful instructions, consistent support and invaluable encouragement at all times.

Numerous contributions and counsel of Mr. Ilhan A. Aksay in the completion of this work were always appreciated. The criticism and comments from Professors Lee F. Donaghey and Richard M. Fulrath were very helpful. Lots of conversations with Mr. Carl E. Hoge are also acknowledged.

Particular thanks are expressed to Miss Kelly Radmilovic and Mr. Neal Houlding for their very warm technical support.

I profitted greatly from the support and assistance of all my fellow students and the staff of the Inorganic Materials Research Division of the Lawrence Berkeley Laboratory.

Finally, I wish to express my countless thanks to my parents, Mr. and Mrs. H. T. Wong; to my brother-in-law and sister, Mr. and Mrs. S. Y. Choi; and to my whole family for their continuous encouragement and consistent support at all times.

This work was done under the auspices of the United States Atomic Energy Commission.

REFERENCES

1. R. E. Herron, C. R. Beecham, and R. C. Padfield, Am. Ceram. Soc. Bull., 46 [12] 1163-68 (1967).

2. R. T. A. Hodson and H. M. Richardson, Trans. Brit, Ceram. Soc., 69 [2] 45-51 (1970).

3. A. P. Raju, I. A. Aksay and J. A. Pask, LBL-159, Nov. 1971.

4. C. S. Smith, Trans. AIME, 175 [1] 15-51 (1948).

5. B. Jackson, W. F. Ford, and J. White, Trans. Brit. Ceram. Soc., 62 [7] 577-601 (1963).

6. D. S. Buist, B. Jackson, I. M. Stephenson, W. F. Ford and J. White, Trans. Brit. Ceram. Soc., 64 [4] 173-209 (1965).

7. B. Jackson and W. F. Ford, Trans. Brit. Ceram. Soc., 65 [1] 19-39 (1966).

8. E. W. Washburn, Phys. Rev. Ser. 2, 17, 273 (1921).

9. I. A. Aksay, C. E. Hoge, and J. A. Pask, to be published in the Journ. Appl. Phys.

10. I. A. Aksay, M.S. Thesis, UCRL-18766, Univ. of California, Mar. 1969.

11. J. White, Materials Science Research, Gray and Frichette Ed., Ch. 5 pp. 96-120 (1969).

12. D. W. Budworth, J. Brit. Ceram. Soc., 4 (4) 481-82 (1967).

13. E. F. Osborn and A. Muan, Fig. 598, Phase Diagrams for Ceramists, E. M. Levin, C. R. Robbins, and H. R. McMurdie, Am. Ceram. Soc., Ohio, 1964.

14. Von H. Tagai, S. Iwai, T. Iseki, and M. S. Tokio, Radex-Rundschau, 4, 577-83 (1965).

15. W. P. Whitney, II and V. S. Stubican, J. Phys. Chem. Solids, Vol. 32, pp. 305-312 (1971).

16. R. A. Swalin, Thermodynamics of Solids, John Wiley & Sons, Inc. (1962).

FIGURE CAPTIONS

1. A meniscus of radius 'R' in a capillary tube of radius 'r'.
2. Schematic of flow through a horizontal tube from one end with other end open to the atmosphere at distance 'h' below the liquid level.
3. Schematic of downward flow through a vertical tube open at bottom end at distance 'h' below the liquid level.
4. Schematic of upward flow through a vertical tube open at top end at distance 'h' below the liquid level.
5. Schematic of flow through a horizontal tube with other end closed.
6. Schematic of downward flow through a vertical tube with bottom end closed at distance 'h' below the liquid level.
7. Schematic of flows from both ends through a horizontal tube at distance 'h' below the liquid level.
8. Schematic of downward and upward flows from top and bottom ends, respectively, through a vertical tube.
9. Schematic of average flow through a vertical tube.
10. Equilibrium of forces acting on the periphery of a contact angle.
11. Wetting behavior and contact angle--a graphical illustration.
12. Schematic of the condition of wetting in the presence of a chemical reaction.
13. Equilibrium of tensions acting at the intersection of a grain boundary and two equivalent solid-liquid interface boundaries.
14. Section through two equal spherical grains in contact with a flat circular grain boundary.
15. Experimental setup for permeation anneal.

16. A representative microstructure of MgO compact as fabricated. (a) 130X, (b) 350X.

17. Log-log relationships of permeation distance of CMS liquid and annealing time at 1550°C.

18. Linear relationships of average horizontal permeation distance with time at 1550°C of different silicate liquids.

19. Log-log relationships of average horizontal permeation distance with time at 1550°C of different silicate liquids.

20. Effect of adjoining large and small channels on penetration distances of liquids with different penetrating rates. (a) slow penetrating liquid, (b) fast penetrating liquid.

21. Effect of R_2O_3 and TiO_2 additions to monticellite on contact angle after 3 hours at 1550°C.

22. A representative microstructure of MgO compact with additional annealing for 2 hours at 1550°C. (a) 130X, (b) 340X.

23. A representative microstructure of MgO compact permeated by a silicate liquid containing 15% Cr_2O_3 after 5 minutes annealing at 1550°C. (a) 130X, (b) 350X.

24. A representative microstructure of MgO compact permeated by a silicate liquid containing 1% Cr_2O_3 after 2 hours annealing at 1550°C. 350X.

25. A representative microstructure of MgO compact permeated by a silicate liquid containing 5% Fe_2O_3 after 2 hours annealing at 1550°C. 350X.

26. A representative microstructure of MgO compact permeated by a silicate liquid containing 1% Al_2O_3 after 2 hours annealing at 1550°C. 350X.

27. A representative microstructure of MgO compact permeated by a silicate liquid containing 10% Al_2O_3 after 2 hours annealing at 1550°c. 350X.

28. A representative microstructure of MgO compact permeated by CMS liquid after 2 hours annealing at 1550°C. (a) 130X, (b) 350X.

29. Cr_2O_3-MgO-CaO•SiO_2 equilibrium phase diagram.

30. Fe_2O_3-FeO-MgO-CaO•SiO_2 equilibrium phase diagram.

31. Al_2O_3-MgO-CaO•SiO_2 equilibrium phase diagram.

32. MgO-R_2O_3 solid solution regions of MgO-MgR_2O_4 systems.

33a. A representative section of the s-l interface of the MgO specimen with a liquid containing 45% Fe_2O_3 after 5 minutes annealing at 1550°C. 140X.

33b. A representative section of the s-l interface of the MgO specimen with a liquid containing 45% Fe_2O_3 after 2 hours annealing at 1550°C. 140X.

34. A representative microstructure of the interior area of the MgO compact of the 45% Fe_2O_3 liquid permeation specimen after 5 minutes annealing at 1550°C, (a) 130X, (b) 350X.

35. A representative microstructure of the interior area of the MgO compact of the 45% Fe_2O_3 liquid permeation specimen after 2 hours annealing at 1550°C. (a) 130X, (b) 350X.

36. Schematic of viscous flow in a straight circular tube.

TECHNICAL INFORMATION DIVISION
LAWRENCE BERKELEY LABORATORY
UNIVERSITY OF CALIFORNIA
BERKELEY, CALIFORNIA 94720